参赛学生姓名:	袁昊琨 嵇海锐
中学:	北京十一学校
省份:	北京市
国家/地区:	中国/北部赛区
指导老师姓名:	于小雨
指导老师单位:	北京十一学校
论文题目:	Theoretical modeling and CFD-based refinement of first-stage thrust characteristics in a two-stage water rocket, supported by experimental measurements

2026 S.-T. Yau High School Science Award
仅用于2026丘成桐中学科学奖公示

Contents

Abstract 1

Chapter 1 Introduction 1

Chapter 2 Literature Review 2

Chapter 3 Experimental Measurements and Data Processing 4

Chapter 4 Numerical Model and Computational Methods 13

Chapter 5 Conventional Formulas and Methods of Comparison 23

Chapter 6 Water Discharge in CFD 26

Chapter 7 Corrections to the Formulas 29

Chapter 8 Effects of Rocket-Acceleration Feedback on Discharge 37

Chapter 9 Discussion 45

Chapter 10 Conclusions 46

References 46

Appendix A Record of Experimental Materials 47

Appendix B Data Acquisition Program 48

Appendix C Experimental Video Materials 48

Appendix D Data Post-Processing Programs 48

Appendix E Flight Measurement Data 48

Appendix F Simulation Data and Animations 48

Appendix G Grid, Time-Step, and Iteration Sensitivity Test Results 48

Acknowledgements 49

2026 S.-T. Yau High School Science Award
仅用于2026丘成桐中学科学奖论文公示

Theoretical modeling and CFD-based refinement of first-stage thrust characteristics in a two-stage water rocket, supported by experimental measurements

Abstract

Water discharge in a water rocket couples compressed-air expansion, liquid acceleration, gas-liquid interface motion, and changes in rocket mass. The conventional models typically use a gas-expansion relation, Bernoulli equation and mass conservation to calculate pressure inside the bottle, nozzle velocity and mass flow rate. These models capture the overall decreases in pressure and discharge velocity, but simplify startup acceleration and late gas-liquid mixing. In this study, a two-stage water rocket was used as an experimental platform. An in-house data logger recorded acceleration, angular velocity, and air pressure during flight. Fixed-camera video was also analyzed in Tracker to compare video-derived axial acceleration with the sensor record. A transient VOF model of the gas-liquid flow inside the first stage was then constructed in Fluent and quantities which are difficult to measure directly in the experiment, such as the pressure, the mass of water, the mass flow rate and the velocity were obtained. Finally, the conventional simplified formulas are examined and corrected individually using the CFD case without rocket-acceleration feedback, and the fitted coefficients are then held fixed to test their applicability in the case with feedback. Three corrections are examined: adding liquid inertia and flow losses to the startup pressure balance, applying separate velocity and mass flow rate coefficients during continuous liquid-phase flow, and accounting for gas mass loss in the pressure relation. After the gas-liquid transition, the outlet velocity is no longer proportional to the mass flow rate, and the pure-liquid approximation fails. For the present cases, acceleration feedback changes the mean pressure, remaining water mass, mass flow rate, outlet velocity, thrust, and acceleration over 0.03-0.14 s, and the full-record thrust integral, by only a few percent. It also changes interface evolution and late transient fluctuations. The original corrections still reduce errors in their respective tests. Agreement in acceleration alone does not validate the pressure, velocity, and mass flow rate relations. Comparing each relation with CFD identifies where errors arise in the calculation of thrust and acceleration.

Keywords: water rocket; gas-liquid two-phase flow; VOF; fluid-rigid body coupling; unsteady flow; simplified theoretical model

1 Introduction

A water rocket uses compressed air to expel water through a nozzle and is propelled by the reaction force of the jet. As more water exits the bottle, the volume of air expands and the pressure drops; over time, the liquid inside the bottle gradually accelerates from rest, while the free surface moves and deforms. Near the end of discharge, air inside the bottle may reach the nozzle before all the water has been expelled and leave together with the water. So a water-discharge process that lasts for less than one second really is an event where the rocket is simultaneously losing weight, the gas is simultaneously expanding, the liquid is flowing, and the gas-liquid interface is simultaneously moving.

There are relatively simple calculation methods used with conventional water rockets. Usually, the internal pressure of the bottle is first determined based on the change of volume of the gas. A Bernoulli equation is then used to derive the nozzle velocity from the pressure difference and continuity relations are utilised to determine the mass flow and the thrust. This way is the method where the overall reductions of the pressure and discharge velocity are taken into account with a few equations. It often, however, treats the flow within the bottle as quasi-steady that is as though the flow were already established at each instant and it assumes that the issuing velocity can be characterized by one mean value. It cannot be determined from the acceleration curve whether this actual water-discharge process meets the requirements during the whole discharging operation.

This is even more important for a two-stage water rocket. The first stage supplies not only the initial thrust, but the velocity and state of motion on subsequent separation and second-stage start up as well. If the first stage

2026 Shanghai High School Science Award 仅用于2026上海市高中生科学奖公示

model is erroneous with regard to time histories of pressure, mass flow rate or thrust, an end result that is seemingly close to the experiment may simply be a canceling of the various errors. This study will thus emphasize relation between physical quantities, and propagation of errors, namely how the pressure inside the bottle changes, how the pressure produces the water-discharge velocity, how this velocity determines mass flow rate and thrust and how these quantities ultimately affect rocket acceleration.

This study merges the flight measurement, Fluent simulation and testing of the conventional formulas. A flight data logging system is invented in-house for the experimental part to take records on acceleration, angular velocity, and Air pressure in actual flight. Fixed-camera video was also processed using Tracker and analysed as an independent measure of the acceleration, to compare with the acceleration derived from the sensor. The time history of the gas - liquid interface, pressure, velocity and mass flow rates in the first-stage were observed numerically using Fluent and the VOF method. In the theoretical analysis, the conventional formulas were broken down into a number of steps, and each step was individually compared with the corresponding CFD data, rather than fitting only the final acceleration output.

In this paper, the authors focus on three questions. First, can first-stage water discharge be divided into phases with distinct flow characteristics? Secondly, where are the principal errors in the conventional formulas in the computation process of pressure, velocity, mass flow rate or thrust? Thirdly, which corrections are useful during which phases and are the necessary corrections applicable when feedback from rocket-acceleration is considered? Because the available high-time-resolution CFD data mainly concern the internal flow of the first stage, and the actual pressure at the beginning of second-stage discharge cannot be measured effectively, the numerical analysis and theoretical corrections in this paper focus mainly on the first-stage propulsion process.

2 Literature Review

2.1 Lumped-Parameter Theory and Conventional Approximations

Prusa derived a simplified water rocket model from conservation relations [1] . Finney analyzed water propulsion as a physics problem and used an isothermal approximation for air expansion inside the bottle [2] . Published water rocket models differ in their assumptions about air expansion, drag, and mass loss. Here, the conventional model calculates gas volume from the remaining water, pressure from a gas-expansion relation, and outlet velocity from the Bernoulli equation.

This model uses a few equations to estimate rocket motion, but reduces the spatially varying flow to mean quantities. A single bottle pressure and a single outlet velocity describe the flow, and the gas- liquid interface geometry is usually omitted. We therefore test the pressure, velocity, and mass flow rate relations separately in each flow phase.

2.2 Unsteady Flow and Gas Thermodynamics

Gommes examined moist-air expansion, transient flow, and liquid inertia, and showed that errors in different model components can cancel, producing apparent agreement with experiments [3] . Romanelli et al. studied air expansion in water rockets, providing a basis for comparing isothermal, adiabatic, and polytropic descriptions [4] . These studies motivate separate tests of the gas-pressure and liquid-flow relations, rather than assigning all deviations to one empirical coefficient.

Johnston analyzed fluid inertance in nonuniform passageways [5] . The conditions in that study are not quite identical with those in a water rocket but one significant concept is applicable here: the velocity of the liquid does not immediately arrive at a constant value when pressure is applied; the flow velocity itself takes time to develop. We therefore test how liquid inertia and flow losses contribute to the startup error of the quasi-steady relation.

The simplified models of Prusa and Finney calculate outlet velocity from the pressure difference without feeding rocket acceleration back into the flow [1, 2] . These simplifications are based on the following approximations: Prusa used the separation between the water-discharge and advection time scales to justify the quasi-steady flow approximation [1] . The OpenMDAO/Dymos water rocket example explicitly assumes that the pressure produced by the water column under $g + a$ is small compared with the gas pressure [6] . For approximately vertical motion, a is the upward acceleration of the rocket, and the effective downward

2026 Siyau High School Science Award
研究2026年度中学科学论文奖

acceleration in the rocket-fixed frame is $g + a$. Neglecting this head requires $\rho(g + a)h$ to be sufficiently small compared with the driving pressure difference over the time interval considered, where h is the liquid-column height. Gommes coupled the motion of the rocket and the liquid and showed that the contribution of apparent gravity caused by rocket acceleration can be of the same order as that of the pressure difference [3].

2.3 The Gas- Liquid Interface and Outlet Flow

The VOF method uses volume fractions to represent the regions occupied by different fluids and is a common method for calculating two-phase flows with free surfaces. Its basic ideas were systematically presented by Hirt and Nichols [7] . The CICSAM method proposed by Ubbink and Issa maintains a sharp gas-liquid interface during volume-fraction transport [8] and corresponds to the volume-fraction discretization scheme actually used in this paper. VOF resolves interface motion and air entry into the outlet, which are omitted from models based only on mean pressure and velocity. In addition, the SST k-ω turbulence model used in this paper was proposed by Menter to describe turbulent effects in near-wall regions and external flows [9] .

Previous water rocket studies have also found that gas may already have entered the nozzle while a small amount of liquid remains inside the bottle [10] . This means that water remaining inside the bottle does not imply that only water is still leaving the nozzle. Once gas- liquid mixing begins, the relationship used to calculate mass flow rate from a fixed water density and a single mean velocity may change. We therefore use the interface evolution to identify when the pure-liquid formulas cease to apply.

Note that discharge experiments with a stationary bottle will, themselves, directly demonstrate that air can reach the nozzle before the water is all discharged. Early air discharge and deformation of the water surface were observed by Watanabe et al., using a thrust stand and high-speed photography [10] . In an experiment with the bottle suspended from a load cell, Yonemoto et al. observed an air column extending from the water surface into the nozzle, while water continued to flow around it [11] . This is key to these observations as it proves that air is vented prior to the complete removal of water under fixed-container operations. In flight, Tomita et al. found the oscillation of the water surface in a funnel shape [12] . In this paper, none of the literature surveyed confirmed the report of air being exhausted prior to complete expulsion of the water during actual flight. Thus any difference in body acceleration should be taken into account when discussing observations made with fixed bottles and observations made with flying rockets.

2.4 Limits of the Observational Evidence

Marranghello et al. demonstrated methods for analyzing the propulsion phase of water rockets using sensors and video [13] . The IMU axes may not align with the rocket's longitudinal axis. The magnitude of the three-axis acceleration therefore cannot simply be treated as the axial propulsion acceleration. When comparing experiment and CFD, the positive direction, treatment of gravity, and time origin must also be made consistent. Accordingly, the experimental part of this study specifically includes sensor bias calibration and extraction of the axial direction.

Note that also flight measurements and measurements of the internal flow need to be distinguished. Even onboard sensors and video measurements by Marranghello et al. and Yang, and Houston [13, 14] were able to measure the movement of the rocket, however, the velocity of the discharge with respect to the nozzle and the mass flow rate cannot be uniquely determined. Quantifying flow amounts from thrust or acceleration would involve extra assumptions, on the pressure, remaining mass and outlet phase distribution. Huang et al. was able to present high-speed imaging of the nozzle discharge and make comparisons between the calculated thrust, pressure and nozzle velocity versus the experimental and CFD results [15] . But the measurement technique discussed is still not adequate to provide nozzle-relative velocity, as well as mass flow rate, simultaneously and independently during flight. As a collection, such studies offer some flow visualization and kinematic measurements, but still there is a lack in the description of the coupled evolution of the internal interface and outlet flow in free flight. Hence it is important to investigate the effect of acceleration feedback on the water-discharge process, and circumstances under which the simplified relations and their fitted corrections hold true.

2026 Siyau High School Science Award
仅用于2026年成都市学科竞赛公示

2.5 Two-Stage Studies and the Position of This Work

Chang and Weng have discussed the flight dynamics of two-stage water rockets [16] . This study also uses a two-stage water rocket as an experimental platform. However, the most complete CFD data currently available concern gas- liquid flow inside the first stage, and the internal pressure at the start of second-stage discharge cannot be obtained accurately. This paper therefore focuses on first-stage propulsion.

2.6 Research Gap and Approach of This Study

Previous studies have examined conventional theory, gas expansion, VOF simulation, and flight measurements. This study compares flight data, CFD results, and conventional formulas through the pressure- velocity- mass flow rate- thrust- acceleration sequence to identify where prediction errors arise.

Accordingly, this study does not aim to fit the final acceleration curve with a large number of parameters. Instead, it makes stepwise comparisons following the physical process: first the relationship between air volume and pressure, then pressure difference and outlet velocity, then velocity and mass flow rate, and finally how these flow quantities produce thrust and acceleration. Each correction is evaluated within its applicable phase, and applications beyond that phase are tested separately; where the data do not distinguish between possible mechanisms, the uncertainty is stated.

3 Experimental Measurements and Data Processing

3.1 Overall Research Framework

The study combines flight measurements, numerical simulation and formula evaluation. Onboard sensors are used to measure rocket acceleration, angular velocity and air pressure. Independent video trials are used to obtain position histories from which axial acceleration is calculated for comparison with the sensor record. Fluent helps to provide the bottle pressure field, velocity field, gas- liquid interface and outlet mass flow rate. Following that, those CFD results are applied in testing the old (conventional) relationship between pressure, velocity, mass flow rate, thrust, and acceleration.



Figure 3-1. Water rocket experimental platform and sensor payload

The platform for the experiment is a two-stage water rocket. The in-house compact logging system is based on the ESP32 microcontroller and uses an independent power supply and local data storage to record the entire flight. The MPU6050 contains 3 axis acceleration and 3 axis angular velocity sensor, the BMP388 is ambient pressure and temperature sensor, and the MicroSD card stores the complete time series. ESP32 is responsible for initialization of the sensors, as well as timed sampling, data calibration, buffer management and data writing. Materials are listed in Appendix A.

3.2 Experimental Platform and Sensor System

3.2.1 Water Rocket Experimental Platform

The water rocket experimental platform is principally composed of four components: these are the launch base, the first stage, the second stage and parachute for nose-cone. For the first stage, you have two beverage

2026 S.T. Yau High School Science Award
仅用于2026丘成桐中学科学奖公示

bottles (that have a nominal volume of 1.25 L) and for the second stage, you have one beverage bottle (with a nominal volume of 1.25 L). The first and second stages are coupled with a pressure triggered separation. The initial water volumes were 625 mL in the first stage and 400 mL in the second stage under the experimental conditions. The experimental records span the entire flight of both stages, and later stages of the CFD analysis are mostly related to the water discharge for the first stage of flight.



Figure 3-2. Launch base

The launch base holds the rocket before launch and is excluded from the flight model.

The dimensions, water volumes, and masses of both stages are inputs to the theoretical calculations and CFD setup. Table 3-1 gives their measured masses.

The nose cone has a parachute to minimize the impact upon landing. However, it did not provide the intended landing protection in the test flights.

Table 3-1. Main mass parameters of the water rocket experimental platform

Item	Mass / kg	Description
Launch base	0.5436	Experimental platform; excluded from flight mass
First-stage dry mass	0.2800	Dry structural mass of the first stage
Second-stage dry mass	0.1123	Dry structural mass of the second stage
First-stage wet mass	0.9050	First-stage dry structural mass plus water mass
Second-stage wet mass	0.5123	Second-stage dry structural mass plus water mass and separator

3.2.2 Sensor Assembly and Hardware Reliability

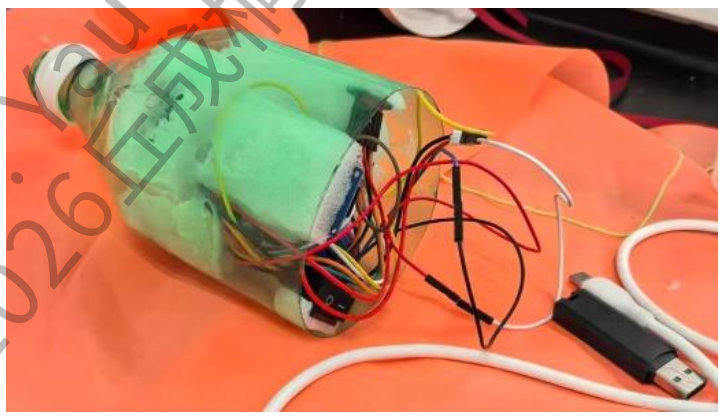


Figure 3-3. Final sensor assembly

After integrating the hardware into the rocket, power-supply, wiring and vibrations issues were discovered: these issues were resolved through hardware changes. An 18650 Lithium battery is used for independent power

2026 S.-T. Yau High School Science Award
仅用于2026丘成桐中学科学奖公示

supply, with the ESP32 to power each module in the final system. Both the MPU6050 and BMP388 utilize the I2C bus, and the MicroSD card is accessed via a specially created SPI bus. This reduces interference between sensor communication and the slower storage process.

The original one was primarily constructed of Dupont jumper wires and pin headers. This was normal during static bench tests, but after rocket installation, the ESP32 reset, or an intermittent loss of sensor contact and/or in-flight recording files occurred because of shaking and/or impact forces. To overcome this, critical power wires and some data wires were subsequently soldered, and mechanical restraints and cushioning materials added to minimise relative movement of wires to the vibration. These changes have resulted in uninterrupted power and continuous data recording during flight testing.

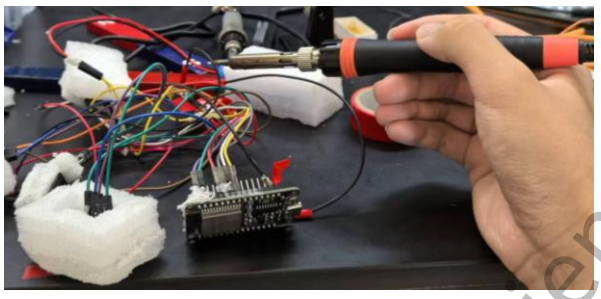


Figure 3-4. Reinforcing sensor connections by soldering

3.2.3 Data Acquisition Program and Storage Design

The sensor system software was developed using the Arduino IDE, and then transferred to the ESP32. On start-up, the program initialises the devices, self-checks, checks for sensor connection, creates files on MicroSD and warms up then calibrates, prior to starting formal data recording. Sampling is scheduled at predetermined times to reduce cumulative timing drift caused by program execution.

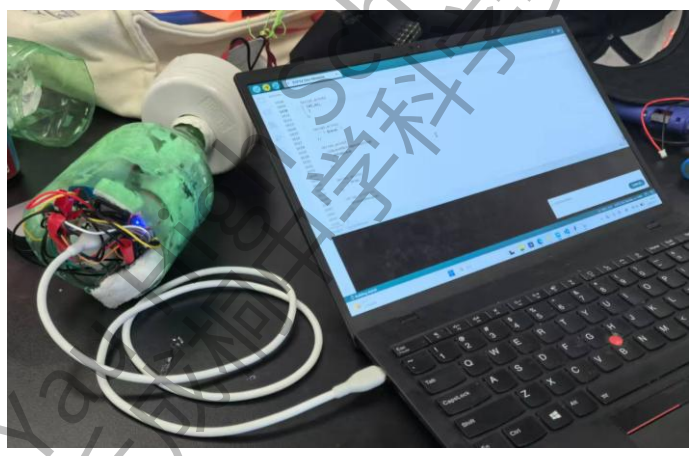


Figure 3-5. Uploading the program to the ESP32 development board through Type-C

In the first program, each sensor read was followed immediately by an SD-card write. A write could block execution for tens of milliseconds, delaying the next sample at the 20 ms sampling interval and potentially causing data loss. The final program separates sampling from writing: one task samples at 50 Hz and queues the records in memory, while another FreeRTOS task writes them to the SD card in batches. The queue absorbs short writing delays.

3.2.4 Warm-Up, Calibration, and Runtime Diagnostics

Another problem was MPU6050 bias and startup drift. The acceleration and angular velocity readings drifted even when the sensor was stationary. Early in the study, a fixed set of zero offsets was estimated from a long static test. Differences were later found between power-up sequences in different environments, however, so each experiment was calibrated separately in the final procedure. The system first warmed up for

2026 T·Yan 青少年科学奖公示 仅用于2026年青少年科学奖公示 Youth Science Awards

approximately 60 s after startup, after which the rocket was kept stationary for approximately 20 s. The average of the data over this interval was taken as the zero reference for that experiment.

$$a_i' = a_i - \bar{a}_i \tag{3-1}$$

Here, i denotes the sensor axis and $\bar{a}_i$ is its mean acceleration over the stationary calibration interval. The same mean-subtraction procedure is applied to each angular velocity component. The acceleration used in post-processing is therefore the change relative to the stationary baseline before launch in that experiment, rather than the unprocessed raw sensor output.

Early test flights also included cases in which the power-on checks were normal but an anomaly suddenly appeared during flight. From the final acceleration curve alone, it was difficult to determine whether the anomaly arose from actual motion or from the recording system. The final program therefore also saves diagnostic variables including time_us, dt_us, dropped, and queue_depth. Here, time_us establishes a common time axis, dt_us checks the actual sampling interval, dropped records the number of records that could not enter the queue, and queue_depth indicates whether SD writing is causing a buffer backlog. These variables allow recording performance to be checked after the experiment.

Table 3-2. Main settings of the final data acquisition program; the complete program is provided in the appendix

Item	Final setting	Description
MPU6050 sampling frequency	50 Hz	Records three-axis acceleration and angular velocity
BMP388 sampling frequency	Target: 50 Hz	Target pressure and temperature update frequency; actual effective updates depend on sensor conversion time
Data logging frequency	Approximately 50 Hz	Each record carries a common timestamp
MPU6050 acceleration range	±16 g	–
MPU6050 angular velocity range	±500 °/s	–
MPU6050 bandwidth	Approximately 44 Hz	Digital filter setting in the program
I^2C interface	SDA GPIO21; SCL GPIO22	Shared by MPU6050 and BMP388
SD memory buffer	Approximately 8 KB	Reduces the effects of frequent card writes
Data queue length	Approximately 1600 records	Absorbs short delays in card writing
Batch writing	Approximately 100 records/batch	Reduces the number of SD write calls
Forced flush interval	Approximately 5 s	Prevents frequent flush operations from blocking the main sampling task
Startup warm-up time	Approximately 60 s	Reduces drift immediately after power-on
Static calibration time	Approximately 20 s	Calculates the zero reference for the current experiment
Total startup preparation time	Approximately 80 s	Sum of warm-up and calibration
MicroSD communication	SPI	Separate from the I^2C sensor bus
SD pins	CS 5; SCK 18; MISO 19; MOSI 23	Final ESP32 wiring
Diagnostic variables	time_us, dt_us, dropped, queue_depth	Check the time axis, dropped records, and buffer status

3.3 Flight Tests

Flight testing was done in an open field. Before each test, the rocket body, interstage structure, and sensor payload were assembled, and the water volumes were then set to the specified values. The sensors were

2026 S. -T. Yau High School Science Award
仅用于2026丘成桐中学科学奖论文公示

warmed up for ~60 s and proceeded with ~20 s stationary recording for bias calibration. Then the rocket was fired at the same conditions as recorded during the test and the full flight was recorded. The initial water volumes were 625 mL in the first stage and 400 mL in the second stage.

The initial amount of water, initial pressure, masses of the individual stages and sensor data files are also stored in the experimental records to aid in the comparing of experimental measurements, CFD running results and theoretical calculations.

Two additional launch records were analysed in Tracker. These launches used the same initial pressure, water mass, rocket configuration, and total mass as the sensor experiment.

We tested for whether or not the ESP32 continued to work after each flight, and for the ability to read all the information in the CSV file from the MicroSD card. Data were only accepted for analysis if the file was readable, time series were not discontinuous, and if there were not any apparent recording faults in the diagnostic variables.



Figure 3-6. Key frames from the flight experiment

The flight videos are listed in Appendix C.

3.4 Sensor Data Post-Processing

The total recording was about 160 s of which only a portion was taken up by flight. The flight interval was chosen based on the examination of propulsion and separation based on the acceleration and angular velocity and the video record.

The final CSV essentially is time_us, dt_us, ax, ay, az, gx, gy, gz, temp, pressure, altitude, dropped, and queue_depth. In this case, time_us is the timestamp, dt_us is the actual time interval between samples. The fields ax, ay, and az contain the calibrated three-axis acceleration, and gx, gy, and gz contain the three-axis angular velocity; the other fields record air pressure, temperature, relative altitude, and acquisition-system status. These time fields provide a means of explicitly checking to see if the actual sampling frequency is near the programmed 50 Hz.

The calibrated acceleration is projected onto the rocket's longitudinal axis. With limited space within the rocket to install the sensor, the x, y, and z axes didn't perfectly coincide with the longitudinal axis of the rocket. It would thus not be possible to use the acceleration along one sensor axis or the magnitude of the three-axis acceleration directly. The components of gravitational acceleration along the three sensor axes will be available on a vertical and stationary rocket and the direction of the longitudinal axis of the rocket will be known in the IMU coordinate system.

$$\boldsymbol{e}_{\parallel} = (0.94456,\ 0.23837,\ -0.22580)$$

$$a_{\parallel,\mathrm{exp}} = \boldsymbol{a}' \cdot \boldsymbol{e}_{\parallel} = 0.94456\ a'_x + 0.23837\ a'_y - 0.22580\ a'_z$$

Here, $\boldsymbol{a}'$ contains the calibrated sensor components from Eq. (3-1), and $a_{\parallel,\mathrm{exp}}$ is their projection onto the rocket axis in the sensor coordinate system. This projection avoids directly treating lateral vibration or sensor mounting-angle errors as acceleration in the propulsion direction.

2026 S. T. Yau High School Science Award
仅用于2026丘成桐中学科学奖论文公示

The complete post-processing code is provided in Appendix D.

3.5 Experimental Data and Recording Stability

We check the flight records for stability and recording faults before selecting data for comparison with CFD and theory. The complete raw data are provided in Appendix E.

3.5.1 Acceleration and Angular Velocity

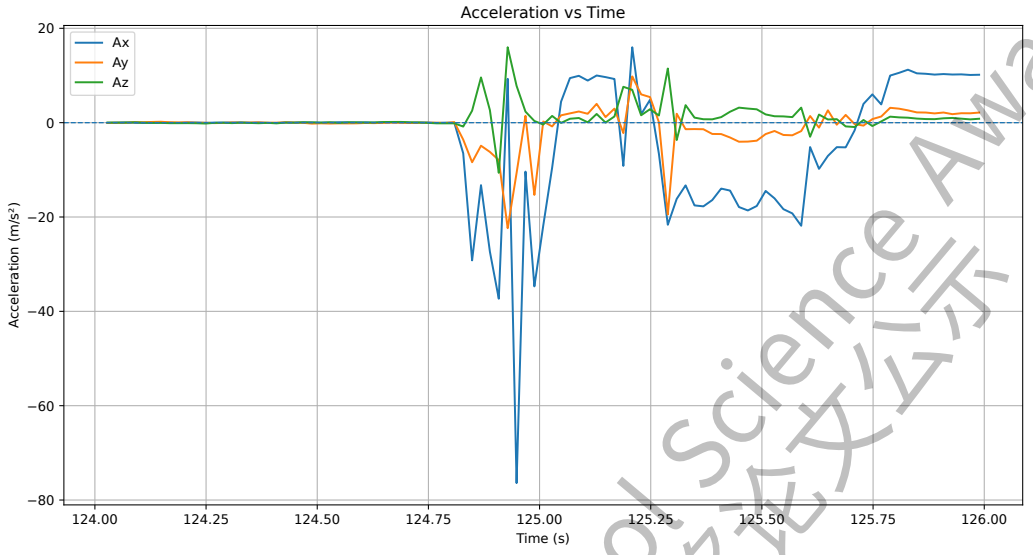


Figure 3-7. Three-axis acceleration records after subtraction of the stationary baseline

The behavior of all three axes during the main flight interval demonstrates unambiguous behavior, with the changes being the greatest along the axis that is closest to the rocket's longitudinal axis. There are two time periods where two main propulsion phases are discernable. Because the sensor axes are not aligned with the rocket axis, the measurements must be projected as described in Section 3.4 before comparison. The curves show changes relative to the stationary pre-launch acceleration baseline.

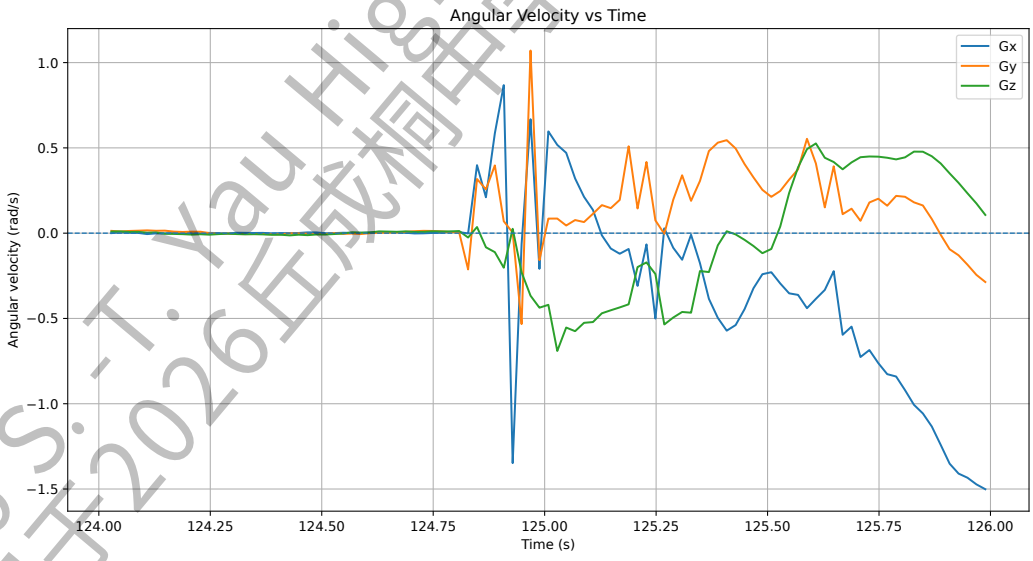


Figure 3-8. Three-axis angular velocity data

2026 S.-T. Yau High School Science Award
仅用于2026丘成桐中学科学奖论文公示

As the rocket flies, it is spinning as shown in the angular velocity records. The x, y, and z components of angular velocity all exhibit significant changes in the vicinity of propulsion and separation, and a certain amount of rotation can be noted thereafter. However, this study does not use the gyroscope data to reconstruct the complete three-dimensional attitude. Angular velocity is instead used primarily as ancillary information to help identify flight states and to discuss the one dimensional modelling limitations.

3.5.2 Limitations of the BMP388 Pressure and Altitude Data

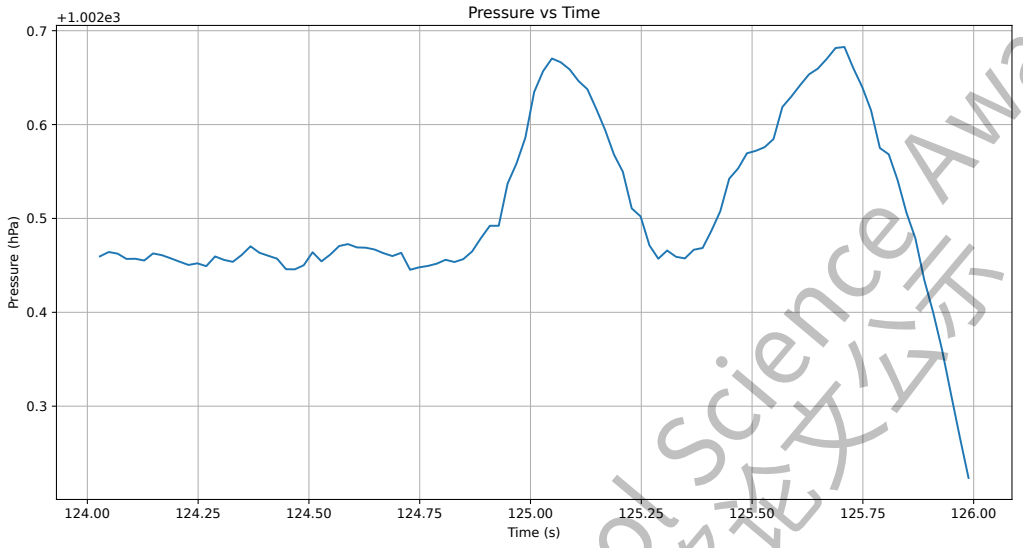


Figure 3-9. Pressure data

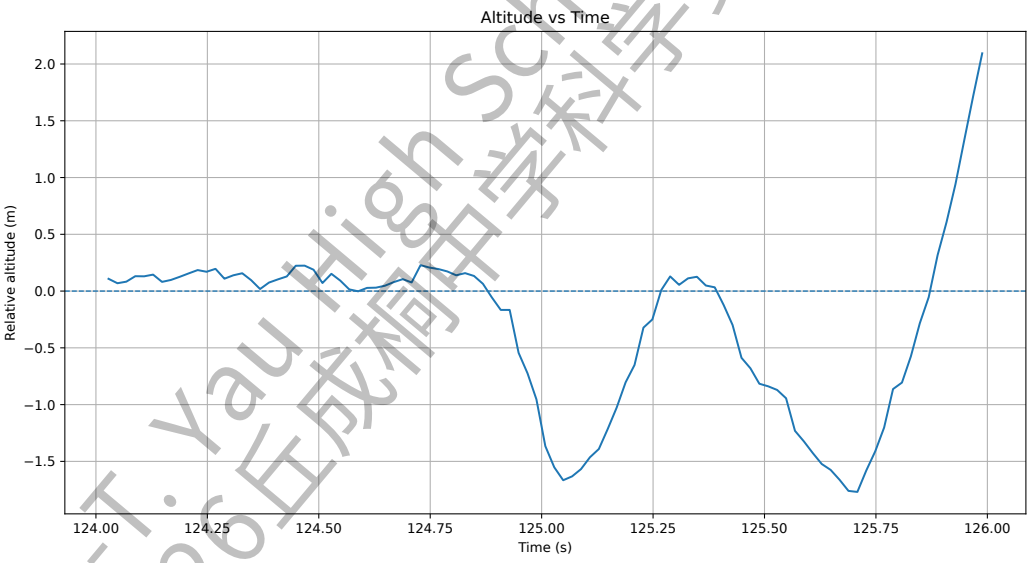


Figure 3-10. Altitude data

2026 S.-T. Yau High School Science Award
仅用于2026丘成桐中学科学奖论文公示

The BMP388 was designed to measure the relative altitude change through atmospheric pressure change. The recorded pressure, though, increases during both periods of main propulsion, leading to quick drops in altitude, followed by quick rises, which are not observed during flight. Therefore, the readings cannot be considered as the ambient static pressure while in propulsion. The sensor may be subject to flow around the rocket, local dynamic pressure and attitude changes. Even when the ambient static pressure changes little, local flow can alter the sensor reading, with a dynamic-pressure contribution of order $\rho_{\text{air}} v^2/2$. These records are thus saved for the sensor installation diagnosis but are not used to calculate the altitude in the propulsion phase.

3.5.3 Sampling Stability and Data Integrity

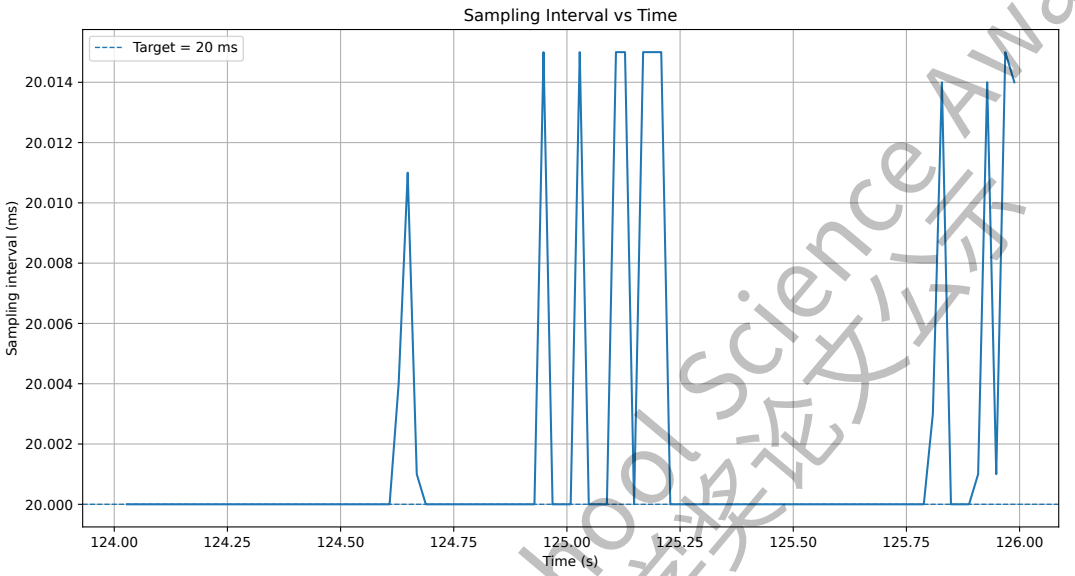


Figure 3-11. Actual sampling interval

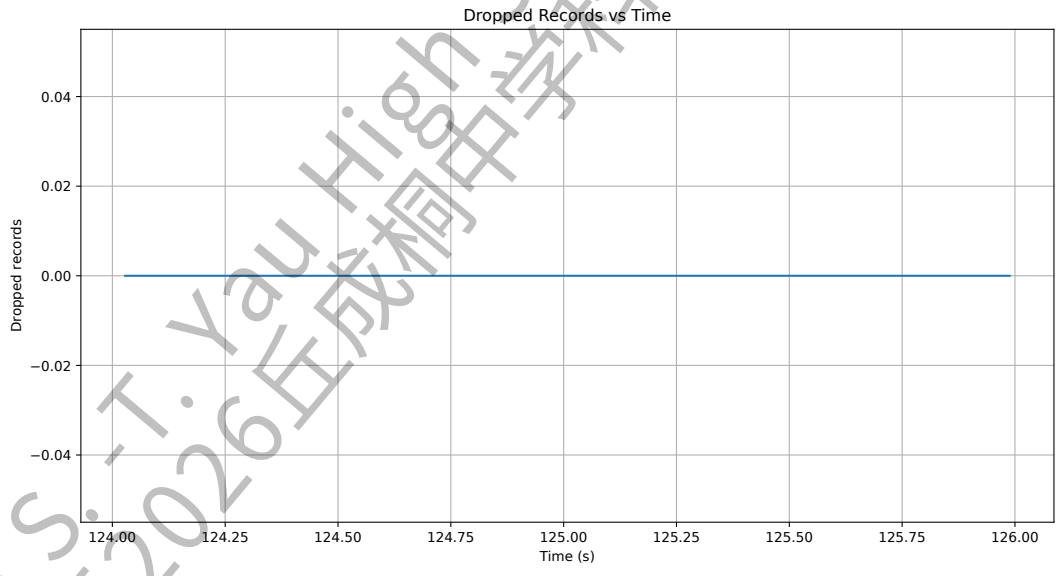


Figure 3-12. Number of dropped records

During flight, dt_us corresponds to a sampling interval of approximately 20 ms, consistent with 50 Hz. The dropped counter remains zero, indicating no records were lost because the queue overflowed. The asynchronous buffer therefore maintained continuous recording during this flight.

2026 S.T. Yau High School Science Award
仅用于2026丘成桐中学科学奖论文公示

3.5.4 Rocket Longitudinal Acceleration

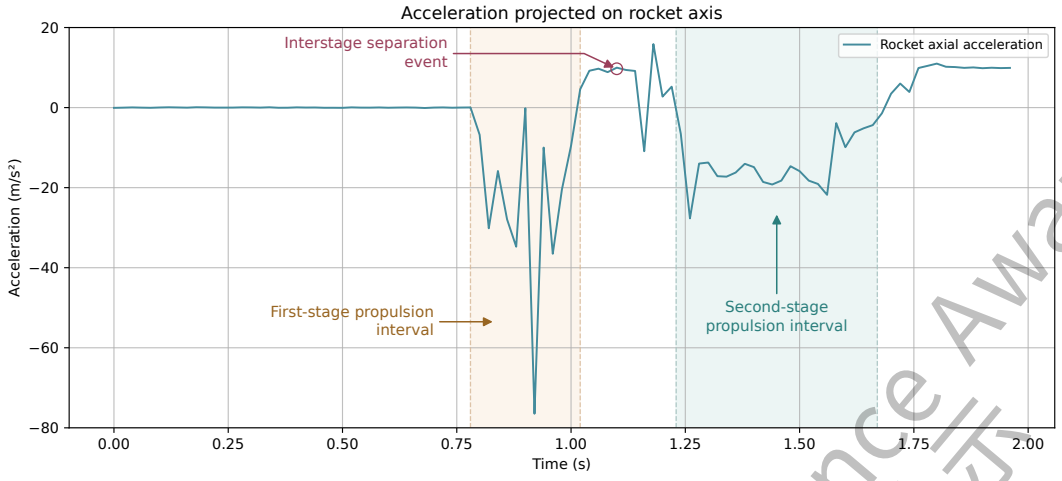


Figure 3-13. Extracted rocket longitudinal acceleration, $a_{\parallel,\mathrm{exp}}$, retaining the sensor-axis sign convention

Projecting the three-axis data onto the direction vector in Section 3.4 gives a rocket longitudinal acceleration more suitable for comparison with the one-dimensional theoretical model. Compared with using an arbitrary single sensor axis, this processing reduces the influence of the sensor mounting angle on the result. The curve contains identifiable features associated with first-stage propulsion, interstage separation, and subsequent changes in flight state.

The sensor sampling period is approximately 20 ms, whereas the CFD time step is much smaller. The sensor data therefore cannot validate the very brief, high-frequency spikes in CFD point by point. The comparison focuses on propulsion duration and the overall acceleration trend.

3.6 Fixed-Camera Video Analysis

Two launches were filmed from a fixed camera position. Yellow tape attached to the rocket provided a visible marker for tracking. The marker positions were processed in Tracker and converted from image coordinates to physical coordinates. Figure 3-14 shows the tracked positions overlaid on a video frame. The frame interval is $\Delta t = 1/60\,\mathrm{s}$, or approximately 16.7 ms, for both videos. The two records contain 19 and 21 position samples, respectively.



Figure 3-14. Tracked rocket positions overlaid on a video frame. Cyan markers show the positions selected in successive frames.

2026 S.-T. Yau High School Science Award
仅用于2026丘成桐中学科学奖论文公示

The acceleration components are calculated using Tracker's finite-difference method. For either coordinate $r = x$ or y,

$$a_{r,i} = \frac{2r_{i+2} - r_{i+1} - 2r_i - r_{i-1} + 2r_{i-2}}{7\Delta t^2}. \tag{3-2}$$

Here, i denotes the central frame. Each estimate spans four frame intervals, approximately 66.7 ms. The fitted rocket-axis angle stored in each project is then used to calculate $a_{\parallel,\mathrm{tr}} = a_x \sin\theta + a_y \cos\theta$, where θ is the signed angle from the positive vertical image axis toward the positive horizontal axis. Positive axial acceleration is directed toward the rocket nose.

The time axes are aligned approximately. The launches were recorded independently, and the launch instant cannot be synchronized precisely with the video frames or the sensor samples. Differences between the video frame interval and the sensor sampling interval further limit alignment. The processed Tracker projects place $t = 0$ at frames 10 and 27, respectively. The comparison therefore emphasizes the overall rise, decay, and end of first-stage acceleration.

Figure 6-1 presents the selected first-stage records. Two sensor points at 0.1100 and 0.1300 s are omitted from the comparison plot. The near-zero value and the following unusually high value were judged physically implausible for this part of the flight: neither is supported by the other experimental records or by order-of-magnitude estimates. The supplier also indicated to the authors that an abnormally high reading may follow a zero reading. The complete records are retained in Appendix E.

4 Numerical Model and Computational Methods

4.1 Objectives of the Numerical Simulation and Model Simplifications

Experiments measure the acceleration and angular velocity of the entire rocket, and the ambient air pressure. During the few hundred millisecond water discharge, however, it is challenging to directly measure the pressure distribution inside the bottle, the motion of the gas-liquid interface, the fluid velocity at the nozzle outlet and the instantaneous mass flow rate. In this study, transient numerical simulation of gas-liquid flow inside the first stage is thus carried out using ANSYS Fluent 2026 R1 Student. The simulation resolves the internal flow that was not measured in the flight tests and provides pressure, velocity, and mass flow rate histories for testing the conventional formulas.

The numerical investigation begins at the moment of start of first-stage water discharge and runs until the main gas-liquid flow has significantly reduced. The approximately axisymmetric bottle and nozzle geometry allows a two-dimensional axisymmetric model, reducing computational cost. Besides the bottle interior, a region of air is kept outside the nozzle and the jet continues to develop upon exiting the nozzle.

The numerical model uses the following assumptions. The bottle walls are assumed to be rigid (no elastic deformation under pressure), water is assumed to have a constant density, air is assumed to be an ideal gas, surface tension is not turned on and the gas-liquid interface is tracked by using VOF. The emphasis is on the general water-discharge process which is dominated by pressure, inertia and mass outflow. We use this model to test the pressure-velocity and velocity-mass flow rate relations in each discharge phase.

4.2 Geometry and Computational Domain

The first stage consists of two connected bottles, each with a nominal volume of 1.25 L. The total internal volume of the computational model is 2.7686 L. As shown in the model, this volume includes the connecting section between the two bottles and the bottle-neck volumes, which are not included in the nominal 1.25 L capacity of each bottle. Its axial profile was first traced from photographs and measured dimensions of the actual bottles, and a two-dimensional axisymmetric computational domain was then constructed. The initial first-stage water volume in the experiment was 625 mL, so the same liquid-water volume was specified during numerical initialization, with air occupying the rest of the bottle. The first-stage axis is taken as the x direction, and the jet leaves the nozzle in the positive x direction.

2026 S. T. Yau High School Science Award
仅用于2026丘成桐中学科学奖论文公示

The geometric model retains the connection between the two bottles, the contracting shoulder region, and the nozzle, and also includes an external air region outside the nozzle. This brings pressure release inside the bottle, acceleration through the nozzle, and the short-distance development of the emerging jet into a single calculation.

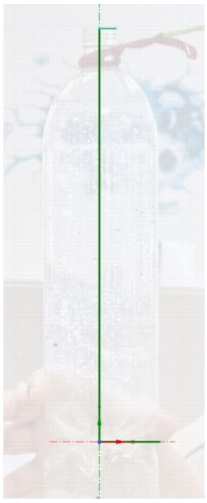


Figure 4-1. First-stage geometry modeling process

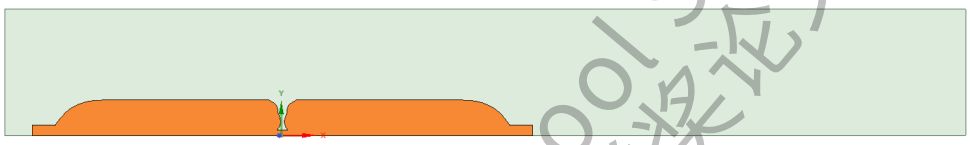


Figure 4-2. Final two-dimensional axisymmetric computational model of the first stage

Table 4-1. Main geometric parameters

Parameter	Value	Source
Total first-stage internal volume	2.7686 L	Full internal model geometry
Initial water volume	0.625 L	Experimental conditions
Initial air volume	2.1436 L	Difference between the two volumes
Nozzle diameter	24 mm	Measurement
Maximum bottle diameter	88 mm	Measurement
Total first-stage length	600 mm	Measurement

4.3 Mesh Generation

An unstructured mesh is used for the computational domain. The largest velocity gradients occur near the contracting bottle shoulder, the nozzle, and the jet, where the gas-liquid interface also moves rapidly. These regions are therefore locally refined. Larger cells are used in the bottle interior away from the nozzle and in the external far field to balance accuracy and computational cost.

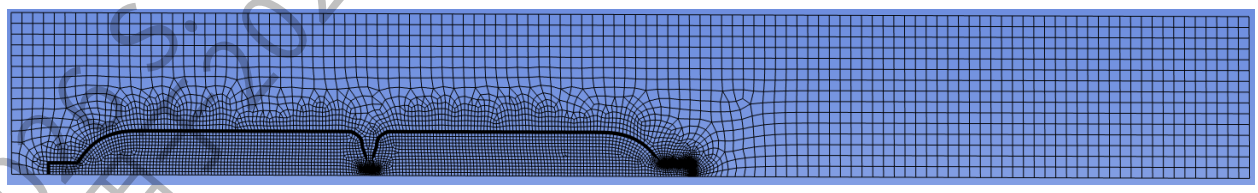


Figure 4-3. Overall computational mesh

2026 T Yau High School Science Award
仅用于2026丘成桐高中科学奖论文公示

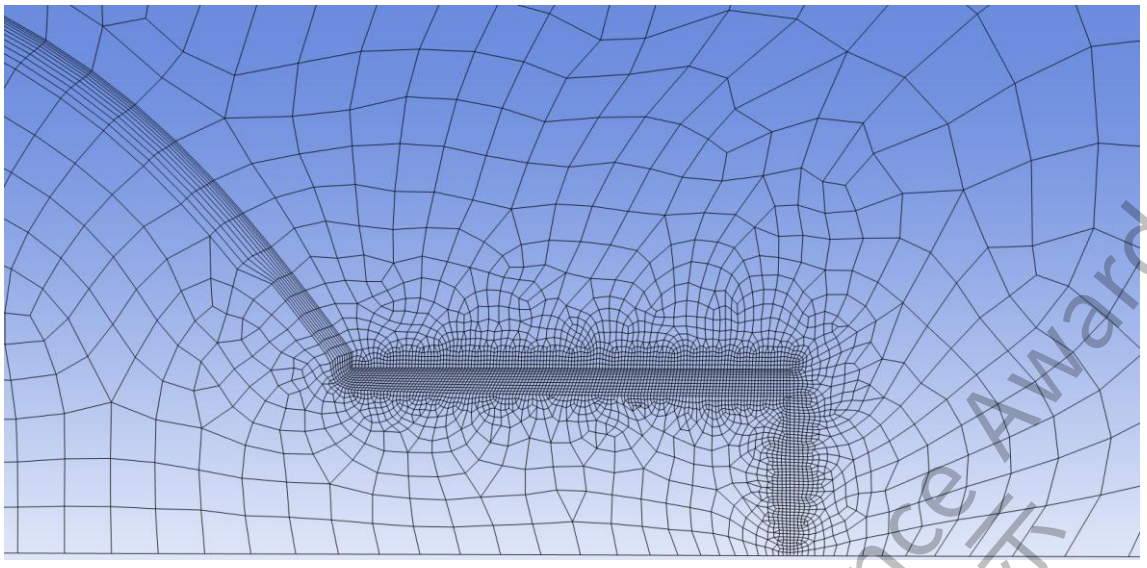


Figure 4-4. Locally refined mesh near the nozzle

Table 4-2. Basic mesh parameters and quality metrics

Item	Value
Total number of cells	12699
Total number of nodes	12850
Mesh size inside the bottle	3 mm
External mesh size	10 mm
Mesh size near the nozzle	0.2 mm
Maximum Skewness	0.84607
Mean Skewness	0.16723
Minimum Orthogonal Quality	0.24912
Mean Orthogonal Quality	0.94551

4.4 Physical Models and Governing Equations

This study uses Fluent's transient pressure-based solver. Since air and water coexist inside the bottle and their interface moves throughout water discharge, the VOF (Volume of Fluid) method is used to describe the gas- liquid two-phase flow. Only the basic equations directly relevant to the analysis in this paper are listed below.

4.4.1 Mass Conservation

The fluid satisfies mass conservation in the computational domain. For transient flow, this can be written as:

$$\frac{\partial \rho}{\partial t} + \nabla \cdot (\rho \boldsymbol{u}) = 0 \tag{4-1}$$

4.4.2 Momentum Conservation

The velocity field is obtained by solving the transient Navier- Stokes momentum equation, which can be written as:

$$\frac{\partial (\rho \boldsymbol{u})}{\partial t} + \nabla \cdot (\rho \boldsymbol{u} \otimes \boldsymbol{u}) = -\nabla p + \nabla \cdot \tau + \rho b \boldsymbol{e}_x \tag{4-2}$$

2026 S. -T. Yau High School Science Award
仅用于2026丘成桐中学科学奖论文公示

Here, $\boldsymbol{u}$ is the local velocity vector, τ is the stress tensor, and $\boldsymbol{e}_x$ points toward the nozzle. The body-force acceleration component is $b = g$ in Case A and $b = g + a$ in Case B, as defined in Section 4.8; both cases retain the unsteady term in the flow equation.

4.4.3 The Gas- Liquid Interface in VOF

The VOF method represents the proportions of water and air in each computational cell using volume fractions. The water and air volume fractions, α_w and α_a, satisfy $\alpha_w + \alpha_a = 1$.

Here, α_w = 1 indicates pure water, α_w = 0 indicates pure air, and cells with 0 < α_w < 1 lie near the numerical gas- liquid interface. The water volume fraction is transported with the flow:

$$\frac{\partial \alpha_w}{\partial t} + \nabla \cdot (\alpha_w \boldsymbol{u}) = 0 \tag{4-3}$$

In mixed VOF cells, density is weighted by the volume fractions of the two phases:

$$\rho = \alpha_w \rho_w + (1 - \alpha_w)\rho_a \tag{4-4}$$

4.4.4 Air Compressibility and the Energy Equation

Water is modeled with a constant density of 998.2 kg/m^3. Air is set to Ideal Gas, allowing its density to vary with absolute pressure and temperature:

$$\rho_a = \frac{p_{\text{abs}}}{RT} \tag{4-5}$$

The Energy Equation is also enabled to describe temperature changes during compressed-air expansion.

4.4.5 Turbulence Model

Large velocity gradients occur near the nozzle, so the SST k-ω turbulence model is used [9] . The model accounts for turbulent stresses near the nozzle and in the external jet.

Table 4-3. Main physical models and material settings

Item	Setting
Solution type	Transient
Solver	Pressure-Based
Spatial formulation	2D Axisymmetric
Multiphase model	VOF
Primary phase	Air
Secondary phase	Water
Turbulence model	SST k-ω
Water density	998.2 kg/m^3
Air density	Ideal Gas
Surface tension	Not enabled
Gravity	9.81 m/s^2, in the +x direction
Energy Equation	Enabled

4.5 Initial and Boundary Conditions

At the initial time, water and air inside the bottle are specified according to the actual experimental conditions. The initial first-stage water volume is 625 mL, and the corresponding region is assigned a water volume fraction of α_w = 1 using Patch. The remaining bottle interior and external computational region are initialized as air, with α_w = 0. The external region is initially at ambient pressure.

Fluent represents absolute pressure as the sum of operating pressure and gauge pressure, $p_{\text{abs}} = p_{\text{op}} + p_{\text{gauge}}$. The initial pressure values are listed in Table 4-4.

2026 S.-T. Yau High School Science Award
仅用于2026丘成桐中学科学奖论文公示

The gauge pressure at the external Pressure Outlet is set to 0 Pa, corresponding to an ambient absolute pressure of approximately 1 atm. Distinguishing gauge pressure from absolute pressure is important because air is modeled as an Ideal Gas and its density is calculated using absolute pressure.

Table 4-4. Initial and boundary conditions

Region/parameter	Fluent setting	Value
Operating Pressure	Operating Pressure	101325 Pa
Initial air pressure inside the bottle	Gauge Pressure	65861.25 Pa
Corresponding absolute pressure	Calculated	167186.25 Pa
Initial water volume	Volume Fraction Patch	625 mL
External boundary	Pressure Outlet	Gauge pressure: 0 Pa
Bottle wall	Wall	No-slip
Axis of symmetry	Axis	-
Initial temperature	Initialization	300 K
Gravity	Enabled	9.81 m/s^2, +x direction

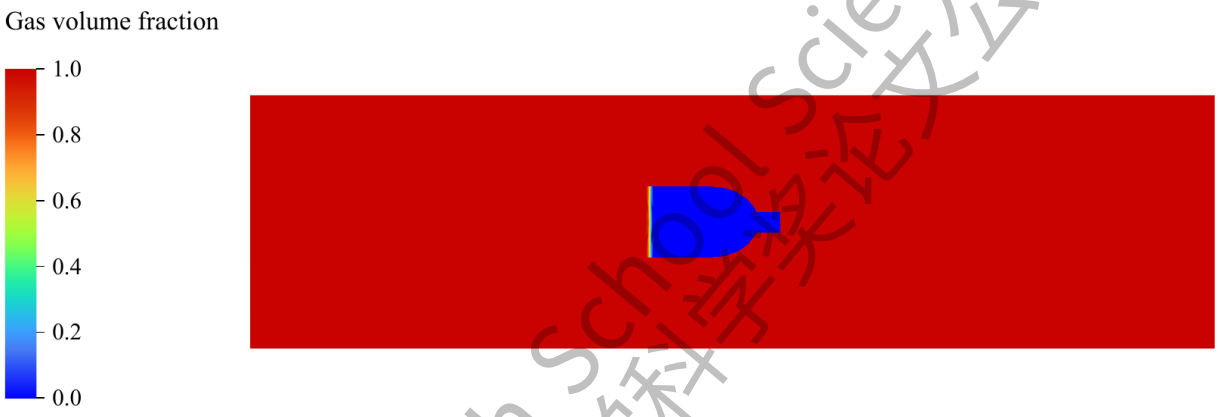


Figure 4-5. Initial air volume fraction distribution

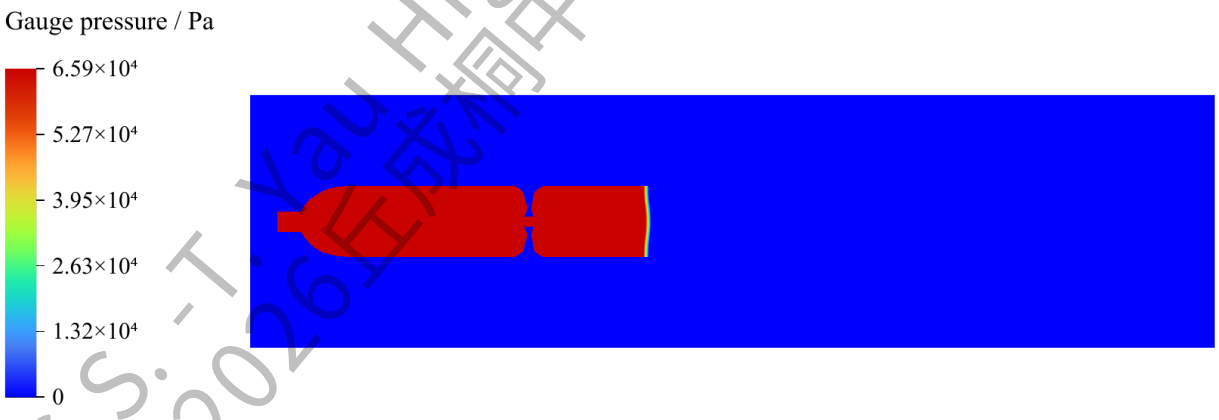


Figure 4-6. Initial static pressure distribution

4.6 Solution Methods and Computational Settings

The numerical solution settings, including CICSAM [8] for volume-fraction discretization, are listed in Table 4-5.

2026 S.-T. Yau High School Science Award
仅用于2026年丘成桐中学科学奖论文公示

Table 4-5. Numerical solution settings

Item	Setting
Pressure-Velocity Coupling	PISO
Gradient	Least Squares Cell Based
Pressure	PRESTO!
Volume Fraction	CICSAM
Momentum	Second Order Upwind
Turbulent Kinetic Energy	Second Order Upwind
Specific Dissipation Rate	Second Order Upwind
Energy	Second Order Upwind
Transient Formulation	First Order Implicit
Maximum iterations per time step	30

4.7 Time Step, Convergence, and Numerical Reliability

In the very short interval after water discharge begins, the liquid inside the bottle rapidly develops flow from rest, and the pressure, nozzle velocity, and gas- liquid interface position change most intensely. To improve the temporal resolution of this startup interval (200 time steps), an initial time step of approximately 1 μs is used. After the first 200 steps, the time step is increased to approximately 10 μs to reduce computational cost.

Within each time step, both equation residuals and key monitored quantities are checked. Residuals below approximately 1×10^{-7}, except for continuity, are used as the main convergence reference. The pressure inside the bottle, outlet mass flow rate, and other quantities are also examined for appreciable drift during the iterations within the same time step. The calculation advances to the next time step only after both have stabilized.

4.8 Simulation Case Settings

The two separate transient VOF simulations are designed to separate deviations in the simplified flow relations from rocket-acceleration feedback effects. Case A is the baseline simulation without this feedback. The second simulation (Case B) takes into account rocket-acceleration feedback. In the above additional case, the body-force acting on the fluid is not constant but during the solution the body-force is changed and there is another calculation of the evolution of pressure, velocity, mass flow rate and the gas- liquid interface.

In Case A, the gravitational acceleration acting on the flow is $g = 9.81\ \mathrm{m/s^2}$ in the positive x-direction. The computed acceleration of the rocket is not part of the flow solution. Case A supplies the reference data for formula comparisons, discharge analysis, and correction fitting; the simplified formulas and this reference CFD case both assume that rocket-acceleration feedback is absent.

Case B uses a non-inertial frame attached to the rocket and represents its axial acceleration through an effective gravity on the fixed mesh. Taking the nozzle direction as positive x, let $a(t)$ denote the upward kinematic acceleration of the rocket, with upward acceleration taken as positive. The inertial body force per unit volume is $-\rho\boldsymbol{a}_b$, in which $\boldsymbol{a}_b$ is the rocket's acceleration vector. Then, the resultant body force and effective gravity are: [3]

$$\begin{aligned} \boldsymbol{a}_b(t) &= -a(t)\boldsymbol{e}_x, \\ \boldsymbol{f}_b(t) &= \rho[g\boldsymbol{e}_x - \boldsymbol{a}_b(t)] = \rho[g + a(t)]\boldsymbol{e}_x, \\ g_{\mathrm{eff}}(t) &= g + a(t). \end{aligned} \tag{4-6}$$

Here, $\boldsymbol{e}_x$ is the unit vector in the nozzle direction. The acceleration $a(t)$ is the kinematic acceleration of the rocket after accounting for gravity. The time-dependent effective gravity is fed back into the flow solution.

Both cases use the geometry and multiphase-flow model described above. Table 4-6 summarizes how each case is used. Case A is used to identify corrections under the baseline assumption, while the additional Case B is used to test the applicability of those corrections when rocket-acceleration feedback is included.

2026 S. T. Yau High School Science Award 仅用于2026年丘成桐中学数学奖公示

Table 4-6. Simulation cases without and with rocket-acceleration feedback

Simulation case	Body-force setting in the flow solution	Role in this study
Case A	$g = 9.81\ \mathrm{m/s^2}$; no rocket-acceleration feedback	Discharge analysis and identification of corrections under the baseline assumption
Case B	$g_{\mathrm{eff}}(t) = g + a(t)$; rocket acceleration fed back into the flow	Comparison of feedback effects and testing of the applicability of the baseline corrections

4.9 Data Monitoring and Definitions of Output Quantities

Fluent saves pressure, water mass, mass flow rate, and mean outlet velocity as functions of time. Thrust and acceleration are calculated from these reports. Each quantity is then compared with the corresponding conventional formula.

4.9.1 Mean Pressure Inside the Bottle and Remaining Water Mass

The pressure condition inside the bottle is represented by the pressure report $P_r(t)$ and it is the mean static pressure within the report region. This amount is noted as the "gauge pressure. The outputs $P_r(t)$ is among the primary ones which will be used later on while testing the air-expansion relation and the pressure-difference-velocity relation.

The amount of the water mass in the bottle is represented by $m_{w,r}(t)$. The obtained by integrating the water volume fraction over the interior of the bottle is:

$$m_{w,r}(t) = \int_{\Omega} \alpha_w \, \rho_w \, \mathrm{d}V \tag{4-7}$$

This quantity directly reflects changes in the amount of water remaining during discharge and can also be compared with the time integral of mass flow rate to check conservation.

4.9.2 Outlet Mass Flow Rate and Mean Velocity

A report surface is defined at the nozzle cross-section to record the mass flow rate $q_r(t)$ through it. The mass flow rate can be written as:

$$q_r(t) = \int_{A_e} \rho \, (\boldsymbol{u} \cdot \boldsymbol{n}) \, \mathrm{d}A \tag{4-8}$$

In Fluent, the mass flow rate sign is relative to the direction of the normal to the report surface. Outflow from the bottle is taken as positive in all plots and formulas.

The area-weighted mean axial velocity at the nozzle outlet is denoted by $u_r(t)$ and is compared with the velocity predicted by the Bernoulli formula.

$$u_r(t) = \frac{\sum_f u_{x,f} A_f}{\sum_f A_f} = \frac{1}{A_e} \int_{A_e} u_x \, \mathrm{d}A. \tag{4-9}$$

4.9.3 Physical Meaning of Thrust

For an ideal one-dimensional jet, a common expression for thrust is:

$$F_T \approx \dot{m} u_e + P_{\mathrm{gauge}} A_e \tag{4-10}$$

In this case, $P_{\mathrm{gauge}} = p_e - p_a$ is the nozzle outlet gauge pressure for which p_e is the nozzle outlet absolute pressure and p_a is the ambient absolute pressure. The first one is due to the momentum of the fluid discharged and the second due to the difference between nozzle exit pressure and ambient pressure.

The force relation in terms of mass flow rate at the outlet q_r, velocity at the outlet u_r and gauge pressure at the nozzle-exit P_{gauge} is:

$$F_r(t) = |q_r(t) u_r(t)| + A_e P_{\mathrm{gauge}}(t). \tag{4-11}$$

2026 S. T. Yau High School Science Award
仅用于2026丘成桐中学科学奖公示

Here, $A_e = 0.00045239\ \mathrm{m}^2$ is the area used in the report expression.

4.9.4 Derived Acceleration

For Case A, the acceleration report before gravity subtraction is obtained by dividing $F_r(t)$ by the instantaneous total mass:

$$a_r(t) = \frac{F_r(t)}{m_{\mathrm{fixed}} + m_{w,r}(t)} \tag{4-12}$$

Here, m_{fixed} represents the structural and payload mass that does not change as water leaves during first-stage discharge (first-stage dry mass + second-stage wet mass + sensor mass, $m_{\mathrm{fixed}} = 0.8205$ kg), and $m_{w,r}(t)$ is the remaining water mass obtained from CFD. Equation (4-12) gives the Case A report before gravity subtraction. With $M_r = m_{\mathrm{fixed}} + m_{w,r}$, the original Case B report already equals $F_r/M_r - g$. The experimental comparison and Section 8 use the kinematic acceleration $a_{\mathrm{kin},r} = F_r/M_r - g$ in both cases.

4.10 Grid Independence Assessment

Grid sensitivity of the simulation is assessed using coarse, medium, and fine meshes containing 10,897, 12,699, and 14,215 cells, respectively. The geometry, boundary conditions, multiphase-flow model, rocket-acceleration feedback, and report definitions are retained across the three simulations. Figure 4-7 shows the computational meshes and nozzle details, and Table 4-7 gives the actual cell counts. For the fixed two-dimensional domain, the effective grid spacing scales as $h \propto N^{-1/2}$, where N is the cell count.

Table 4-7. Meshes used in the grid sensitivity assessment

Grid	Cell count N	Change from medium	h/h_M
Coarse (C)	10,897	−14.19%	1.0795
Medium (M)	12,699	0%	1.0000
Fine (F)	14,215	+11.94%	0.94517

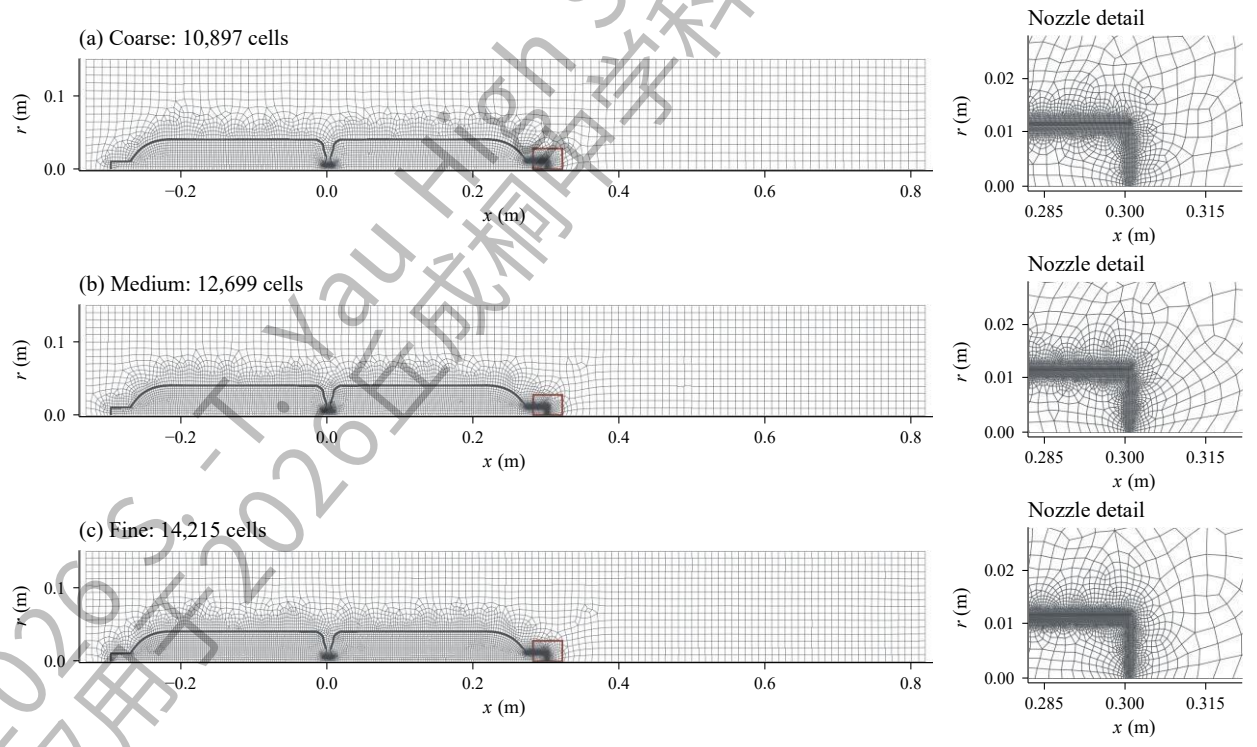


Figure 4-7. Coarse, medium, and fine meshes. The red rectangles mark the nozzle regions enlarged in the right-hand panels. All meshes are shown at the same physical scale.

2026 S.-T. Yau High School Science Award
仅用于2026丘成桐中学科学奖文公开

The comparison uses the first 500 time steps of each simulation: 200 steps of 1 μs, followed by 300 steps of 10 μs, covering $0 \le t \le T = 3.20$ ms. The quantities compared are bottle gauge pressure P_r, mean outlet velocity u_r, outlet mass flow rate q_r, cumulative discharged water $\Delta m_w(t) = m_{w,r}(0) - m_{w,r}(t)$, derived thrust F_r, and kinematic acceleration $a_{\mathrm{kin},r}$.

For a quantity ϕ, the time-weighted root-mean-square difference $D_\phi^{i,j}$ and its normalized value $E_\phi^{i,j}$ are defined as

$$D_\phi^{i,j} = \left[\frac{1}{T}\int_0^T (\phi_i(t) - \phi_j(t))^2 \,\mathrm{d}t\right]^{1/2},$$
$$E_\phi^{i,j} = \frac{D_\phi^{i,j}}{\left[\frac{1}{T}\int_0^T \phi_j^2(t)\,\mathrm{d}t\right]^{1/2}} \times 100\%. \tag{4-13}$$

Here, j denotes the finer mesh in each pair. The integrals are evaluated by the trapezoidal rule on the original time axis, so the two time-step sizes are weighted by their duration.

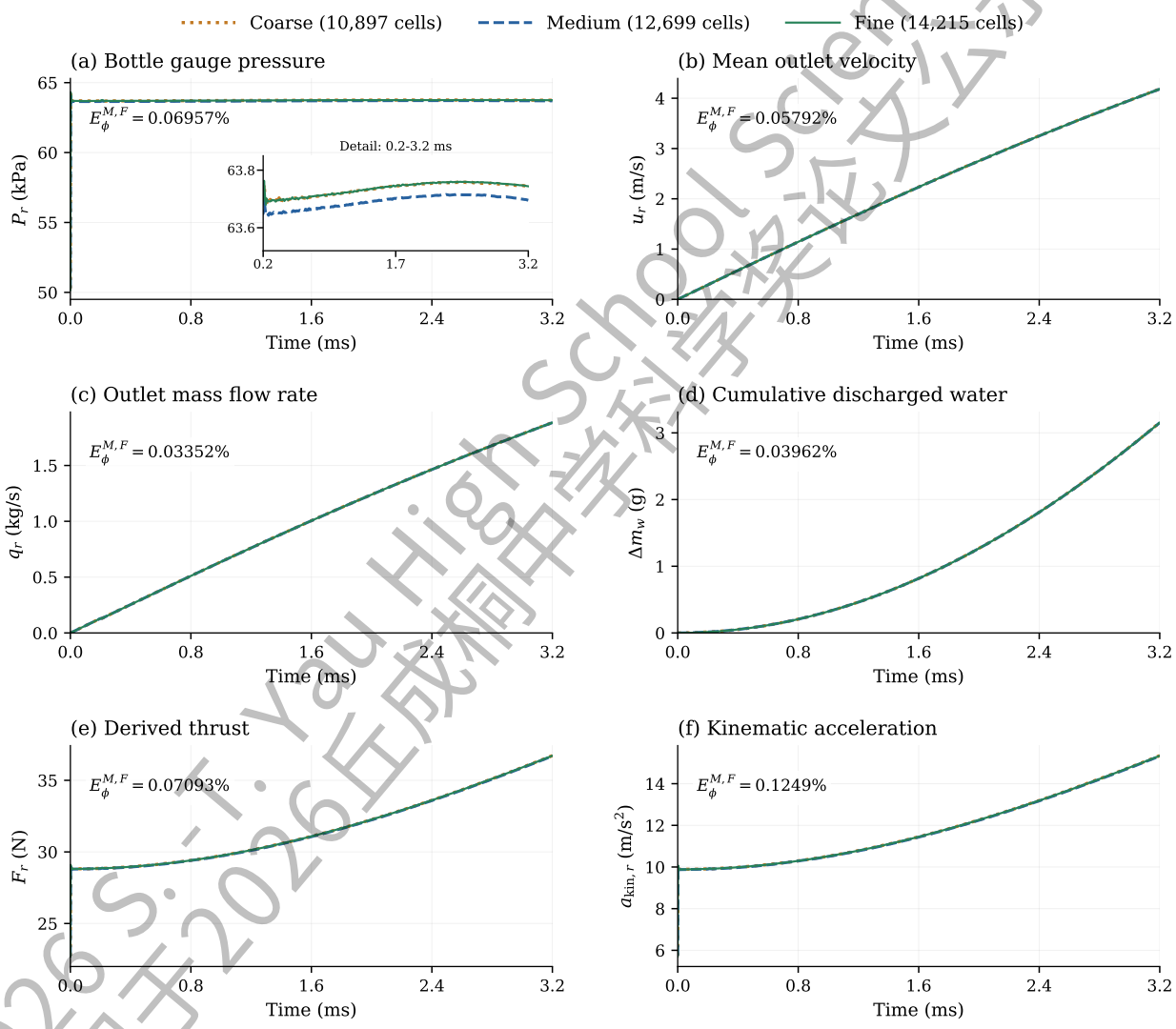


Figure 4-8. Comparison of the first 500 time steps on three meshes for Case B. The inset resolves the small pressure differences. The percentages give the medium- fine normalized RMS differences defined by Eq. (4-13).

2026 S.-T. Yau High School Science Award
仅用于2026丘成桐中学科学奖论文公示

The three meshes give closely overlapping time histories (Figure 4-8). The normalized RMS differences for all six quantities remain below 0.15% in both adjacent-grid comparisons (Table 4-8). At $T = 3.20$ ms, the discharged water masses are 3.1548, 3.1527, and 3.1538 g on the coarse, medium, and fine meshes, respectively; the medium- fine difference is 0.03488%.

Table 4-8. Time-weighted differences over 0- 3.20 ms. The RMSE column gives $D_\phi^{M,F}$ in the unit listed for each quantity.

Quantity (unit)	$E_\phi^{C,M}$ (%)	$E_\phi^{M,F}$ (%)	RMSE (M- F)
Pressure P_r (Pa)	0.06776	0.06957	44.34
Velocity u_r (m/s)	0.08975	0.05792	0.001448
Mass flow rate q_r (kg/s)	0.06269	0.03352	0.0003772
Discharged water Δm_w (g)	0.06743	0.03962	0.0005662
Derived thrust F_r (N)	0.07541	0.07093	0.02251
Acceleration $a_{\mathrm{kin},r}$ (m/s^2)	0.1423	0.1249	0.01493

These results indicate that the simulation is insensitive to the grid changes examined.

4.11 Time-Step and Iteration Sensitivity Assessment

Two additional calculations on the mesh used in this study assess sensitivity to the time-step size and the maximum number of iterations per time step. The geometry, boundary conditions, physical models, rocket-acceleration feedback, and report definitions are retained. One calculation increases the iteration limit from 30 to 60 while retaining the original time steps. The other halves both time-step sizes while retaining the limit of 30 iterations per step (Table 4-9).

Table 4-9. Settings used in the time-step and iteration sensitivity assessment. All calculations cover 0- 3.20 ms.

Calculation	Time step (μs)		Maximum iterations	Time steps
	0- 0.20 ms	0.20- 3.20 ms	per time step	
Baseline	1	10	30	500
Increased iteration limit	1	10	60	500
Halved time step	0.5	5	30	1000

The baseline and increased-iteration calculations each contain 200 initial steps and 300 subsequent steps. The half-time-step calculation contains 400 initial steps and 600 subsequent steps, so all comparisons cover the same physical interval, $0 \le t \le T = 3.20$ ms. The six quantities and time-weighted difference measures are the same as in Section 4.10 and Eq. (4-13). Here, the reference j is the calculation with an iteration limit of 60 per step or with halved time steps. For the time-step comparison, the baseline values are linearly interpolated to the finer time coordinates before trapezoidal integration.

The three calculations give closely overlapping time histories at the scale of the full comparison interval (Figure 4-9), with only small local differences during the initial pressure rise.

Table 4-10. Time-weighted differences over 0- 3.20 ms. RMSE is given in the unit listed for each quantity; E_ϕ is the normalized RMS difference.

Quantity (unit)	30 vs. 60 iterations		Δt vs. $\Delta t/2$	
	E_ϕ (%)	RMSE	E_ϕ (%)	RMSE
Pressure P_r (Pa)	0.06870	43.78	0.1279	81.51
Velocity u_r (m/s)	0.03737	0.0009342	0.1648	0.004112
Mass flow rate q_r (kg/s)	0.03656	0.0004115	0.1717	0.001933
Discharged water Δm_w (g)	0.04109	0.0005873	0.09869	0.001411
Derived thrust F_r (N)	0.06900	0.02190	0.1139	0.03615
Acceleration $a_{\mathrm{kin},r}$ (m/s^2)	0.1254	0.01499	0.2069	0.02473

2026 Si-Yuan High School Science Award 仅用于2026四源中学科学奖公示

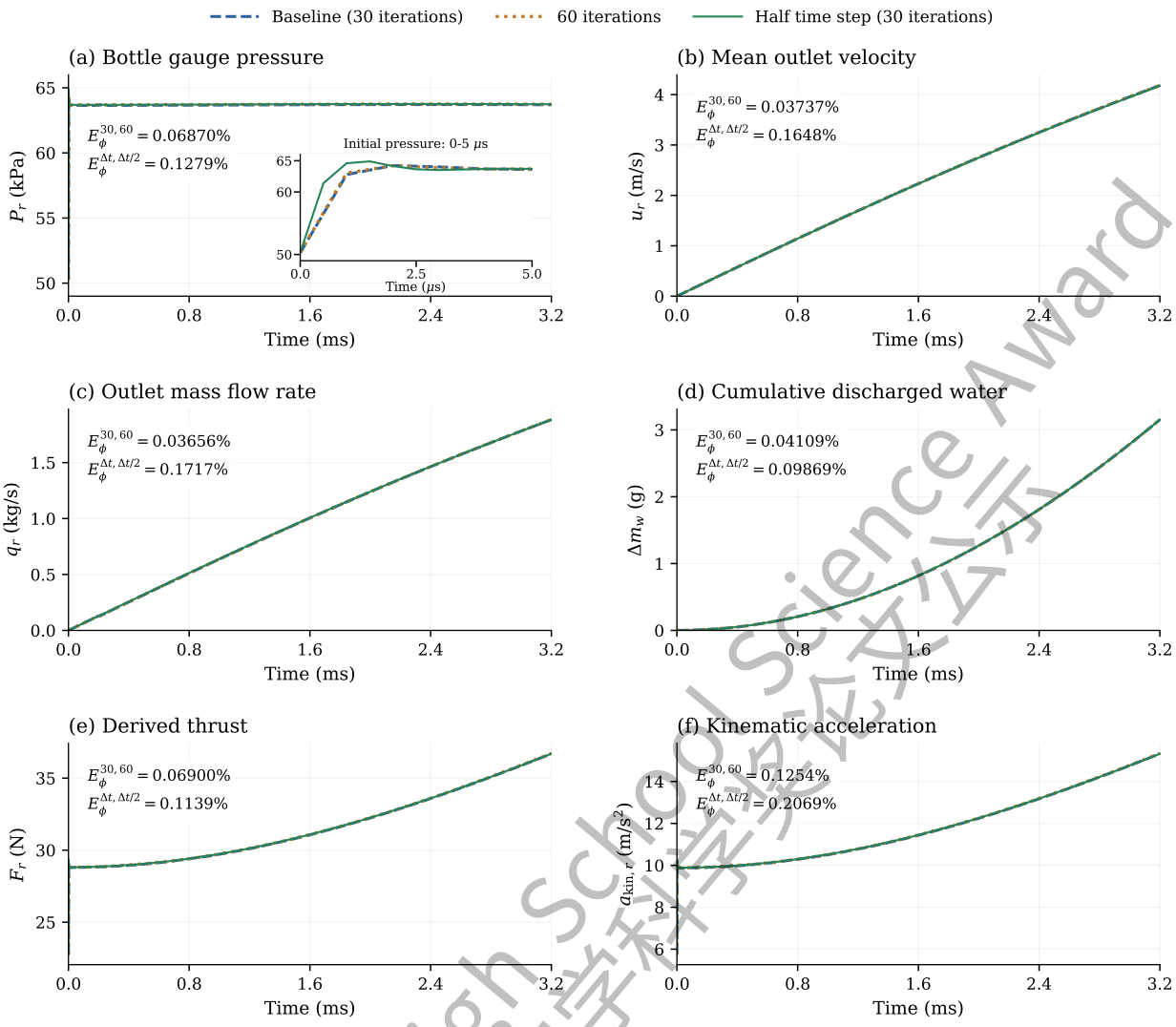


Figure 4-9. Time-step and iteration sensitivity of Case B over 0- 3.20 ms. The inset resolves the initial pressure rise over 0- 5 μs. The labels give normalized RMS differences for the 30- 60 iteration-limit comparison and the original- halved time-step comparison. Iteration counts in the legend denote the maximum per time step.

These comparisons indicate that the quantities are insensitive to the tested time-step sizes and iteration limits and support retaining the original time steps and a maximum of 30 iterations per time step.

5 Conventional Formulas and Methods of Comparison

The preceding experiments and simulations provide two types of information: the sensors record the motion of the rocket body, while CFD records changes in the internal fluid. We next use the CFD pressure, velocity, mass flow rate, and water mass to examine each step of the conventional formulas. We seek to identify which assumptions become inappropriate, when this happens, and which corrections can explain the original deviations.

5.1 CFD Data and Notation

The Case A CFD reports contain 23 678 time points over 0- 0.23497 s. Outlet velocity is denoted by u to avoid confusion with the flight velocity of the rocket body, and mass flow rate is denoted by q, in kg/s.

2026 S.T. Yau High School Science Award
仅用于2026丘成桐中学科学奖论文公示

Table 5-1. Main symbols used in the following sections

Symbol	Meaning	Unit
P_r	Bottle-surface area-averaged gauge pressure report	Pa
P_{gauge}	Nozzle outlet gauge-pressure report from CFD	Pa
P_g, P_a	Absolute gas pressure and ambient absolute pressure in the formulas	Pa
u_r, q_r	CFD velocity and mass flow rate reports	m/s, kg/s
$m_{w,r}$	CFD water mass	kg
V_g, V_b	Gas volume and total internal bottle volume	m^3
A, A_b	Nozzle area and bottle cross-sectional area used in Eq. (5-3)	m^2
ρ_l	Liquid-water density	kg/m^3
H, H_0	Prescribed liquid head and initial head, $H_0 = 0.155$ m	m
g	Gravitational acceleration, $g = 9.81$ m/s^2	m/s^2
F_r	Derived force from the CFD reports	N
a_r	Case A acceleration report before gravity subtraction	m/s^2
a_{exp}	Experimental axial acceleration, with upward acceleration positive	m/s^2
$a_{\text{kin},r}$	CFD kinematic acceleration, $F_r/M_r - g$	m/s^2
$a_{\text{kin,calc}}$	Calculated kinematic acceleration, $F_{\text{calc}}/M_r - g$	m/s^2
P_{calc}, ΔP	Calculated bottle gauge pressure and driving gauge pressure supplied to the velocity relation	Pa
M_r	Total mass used in the comparisons, $m_{\text{fixed}} + m_{w,r}$	kg
b	Body-force acceleration toward the nozzle: g in Case A and $g + a$ in Case B; $b = g_{\text{eff}}$ in Case B	m/s^2
A_e	$A_e = A$ is the nozzle area used in Eq. (4-11).	m^2

The subscript r identifies CFD report values, calc calculated values, and exp experimental values. The subscript kin identifies acceleration after gravity subtraction. The outlet pressure report is denoted by P_{gauge}.

5.2 Basic Assumptions and Calculation Relations of the Conventional Model

The conventional formulas first assume that the space inside the bottle is occupied only by water and air. Each volume of water discharged produces an equal increase in air volume. Thus, once the remaining water mass is given, the gas volume is

$$V_g = V_b - \frac{m_w}{\rho_l}. \tag{5-1}$$

Assuming that no gas leaves the bottle and that its expansion is approximately adiabatic gives

$$P_g = P_{g0}\left(\frac{V_{g0}}{V_g}\right)^{\gamma} \qquad \gamma = 1.4. \tag{5-2}$$

Here, P_{g0} and V_{g0} are the initial absolute gas pressure and gas volume.

The second step converts the pressure difference and gravitational head into outlet velocity using the Bernoulli relation. The initial liquid head is 0.155 m and is assumed to decrease linearly with the remaining liquid volume; gravitational acceleration is 9.81 m/s^2. The bottle-to-nozzle area correction from continuity is retained:

$$\begin{aligned} H(t) &= H_0\frac{V_w(t)}{V_w(0)} = 0.155\frac{m_{w,r}(t)}{m_{w,r}(0)}\ \text{m}, \qquad g = 9.81\ \text{m/s}^2, \\ \beta_A &= 1 - \left(\frac{A}{A_b}\right)^2, \qquad u_B = \sqrt{\frac{2[(P_g - P_a) + \rho_l g H(t)]}{\rho_l \beta_A}}. \end{aligned} \tag{5-3}$$

2026 S. T. Yau High School Science Award
仅用于2026丘成桐中学科学奖论文公示

Here, u_B is the outlet velocity calculated using the original formula. The subscript B denotes the Bernoulli baseline, not simulation Case B. In this experiment, β_A is approximately 0.99447, close to 1, so this geometric correction is small. Equation (5-3) assumes that the outlet velocity adjusts instantaneously to the driving pressure.

The third step treats the nozzle as a liquid cross-section with uniform velocity and density to obtain the mass flow rate, and then calculates the remaining water mass from the cumulative outflow:

$$q_B = \rho_l A u_B \qquad m_{w,B}(t) = m_{w0} - \int_0^t q_B(\tau)\,\mathrm{d}\tau. \tag{5-4}$$

The conventional model calculates thrust and acceleration before gravity subtraction as follows:

$$F_B = q_B u_B \qquad a_B = \frac{F_B}{m_{w,B} + m_{\text{fixed}}}. \tag{5-5}$$

Equation (5-5) gives the conventional momentum-thrust expression, with $m_{\text{fixed}} = 0.8205\ \text{kg}$. In the subsequent relation-by-relation comparisons, the simplified model also includes a pressure-thrust term. Because it cannot predict nozzle-exit pressure independently, it approximates the nozzle-exit gauge pressure by the calculated bottle gauge pressure, $P_{\text{gauge,calc}} \approx P_{\text{calc}}$, and evaluates $F_{\text{calc}} = |q_{\text{calc}} u_{\text{calc}}| + A_e P_{\text{calc}}$. The acceleration denominator is the sum of the CFD remaining water mass and m_{fixed}.

5.3 Model Decomposition and Analysis of Error Sources

If pressure, velocity, and mass flow rate are calculated together and only acceleration is checked, errors from the preceding steps become mixed. For example, a mass flow rate that is too high and a velocity that is too low may still produce a product close to CFD. We therefore examine the relations separately before attempting to combine them.

Table 5-2. Separate tests of the conventional formulas

Relation tested	Input read from CFD	Quantity calculated from formulas
Gas-expansion relation	Water mass and corresponding gas volume	Pressure
Pressure-difference- velocity relation	Pressure and water mass for H	Outlet velocity
Velocity- mass flow rate relation	Outlet velocity	Mass flow rate
Startup inertia relation	Velocity change and water mass for H	Required pressure difference
Combination of several formulas	Water mass as input to pressure and H	Pressure, velocity, mass flow rate, and a cumulative water-quantity check

5.4 Evaluation of the Corrections

The curves are first compared to see if they are too high, too low or if they differ in trend within a phase; the differences are summarized by numerical errors. The adopted measure is the root mean square error (RMSE), which quantifies the difference between the calculated and CFD curves; lower values indicate closer agreement. Because the CFD time step varies throughout the record, the calculation was weighted by the length of the intervals:

$$\mathrm{RMSE}_x = \sqrt{\frac{1}{T}\int_{t_a}^{t_b} [x_{\text{calc}}(t) - x_r(t)]^2\,\mathrm{d}t}, \qquad T = t_b - t_a. \tag{5-6}$$

If several variables are combined, the error for each one of them is first normalized by dividing the error for each variable by its full-record range, defined as the difference between its maximum and minimum values, and

2026 S. T. Yau High School Science Award
仅用于2026丘成桐中学科学奖论文公开

then combining the errors to compare. This avoids "overloading" pressure because of the size of the numbers. The pressure, water mass, mass flow rate and velocity are all assigned equal weights, while lower weights are assigned to the force and acceleration computed from these.

The correction must simultaneously lower the numerical error in the field and not bring about physical inconsistencies like negative mass.

6 Water Discharge in CFD

6.1 Comparison of Experimental and CFD Acceleration

The onboard-sensor record, the two Tracker trials and the two CFD Cases A and B can be seen in figure 6-1; both of the video trials indicate a rise in the acceleration followed by the overall decrease. Their greatest values are: 40.94 m/s² and 45.58 m/s². Both turn negative between the samples at 0.2000 s and 0.2167 s, and move down to ~-9 m/s² at 0.2333 s. The CFD curves also tend to negative acceleration, closer to the end of the simulated timeframe. The sensor data has wider local fluctuations, but also ends in the negative acceleration.

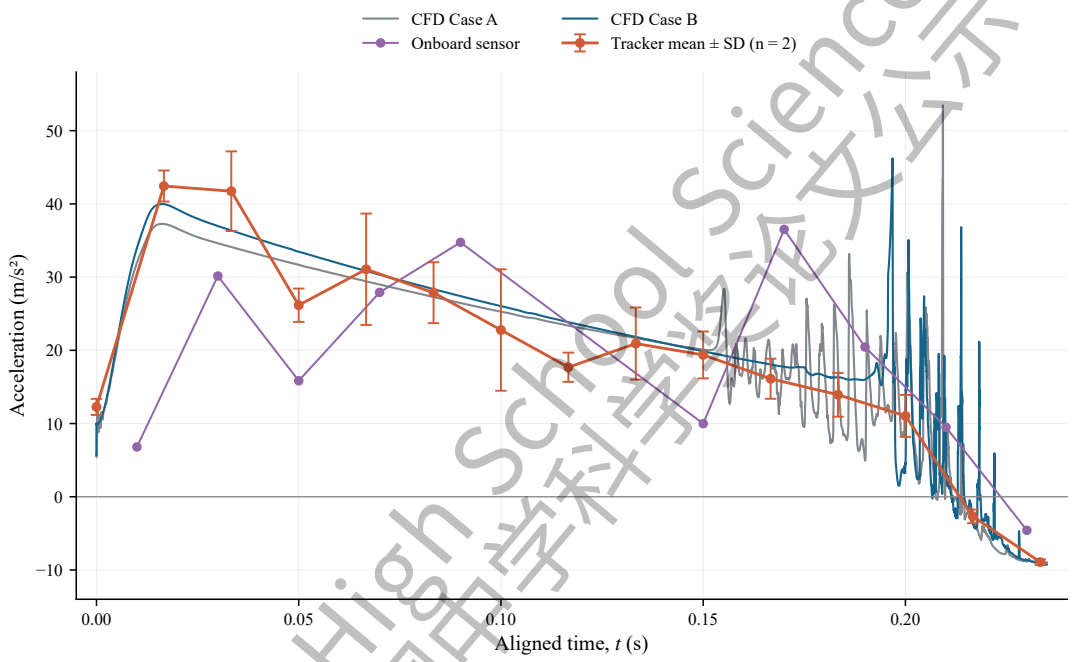


Figure 6-1. First-stage acceleration from the onboard sensor $a_{exp} = -a_{\parallel,exp}$, the mean of Tracker trials 1 and 2, and CFD Cases A and B $a_{kin,r}$. Error bars show ±1 sample standard deviation across the two Tracker trials (n = 2). Experimental acceleration is positive along the rocket axis; CFD acceleration is positive upward. Time alignment is approximate.

The video results provide a second measurement method for checking the broad first-stage acceleration trend. The three experimental records are not perfectly aligned in time. Their differences may reflect launch-to-launch variation and errors in position and angle estimation.

6.2 Time Evolution of Flow Variables and Division into Phases

Figure 6-2 shows the Case A CFD time histories. Pressure is already present at startup, while velocity and mass flow rate rise from values near zero. During the subsequent continuous liquid-phase interval, pressure, velocity, and mass flow rate decrease smoothly. Velocity and mass flow rate fluctuations increase after approximately 0.152 s. At later times, an increase in velocity does not necessarily produce an increase in mass flow rate.

2026 S.T. Yau High School Science Award
仅用于2026丘成桐中学科学奖论文公示

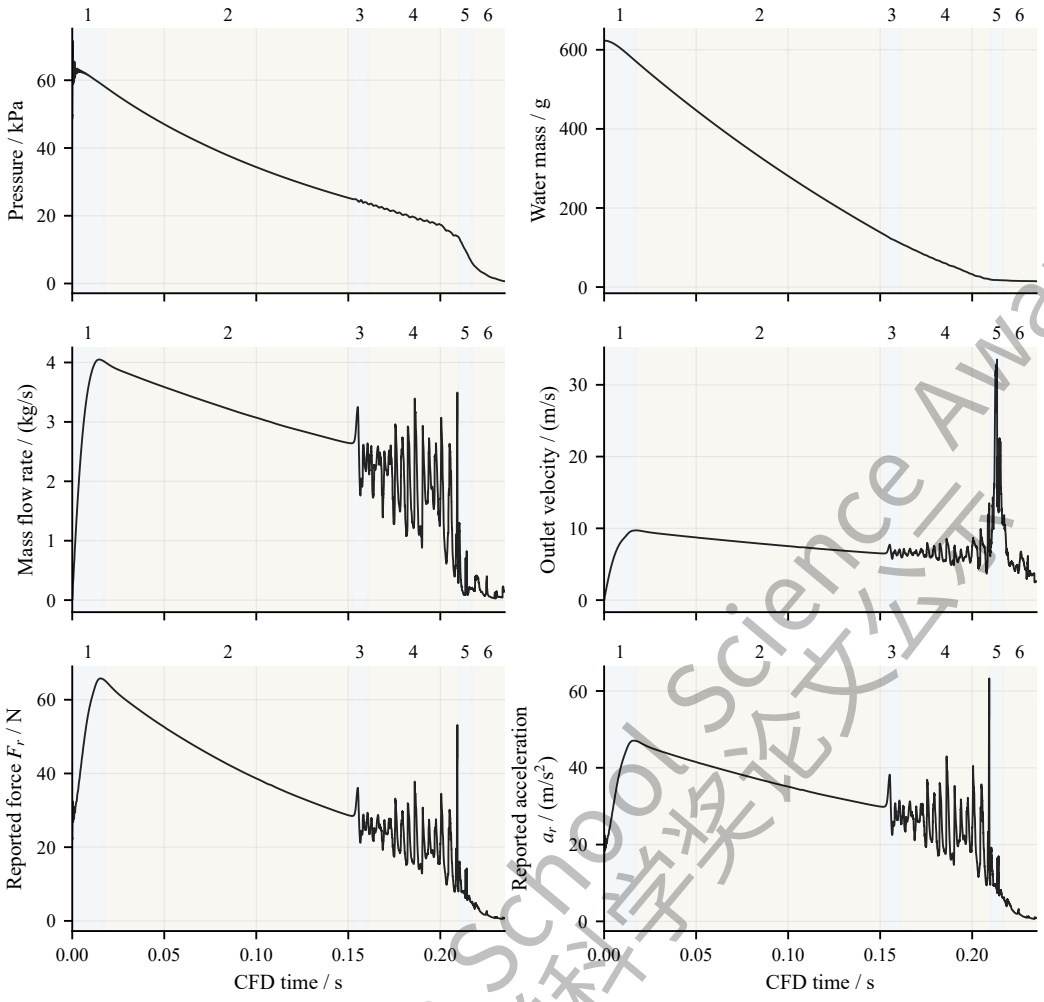


Figure 6-2. Original CFD pressure, water mass, mass flow rate, velocity, reported force, and acceleration before gravity subtraction in Case A. The background marks the six analysis phases

To examine these changes separately, we divide the analysis into six time intervals.

Table 6-1. Six flow phases in Case A

Phase	Time interval / s	Main features
1 Startup	0- 0.0174	Pressure is established; liquid velocity and mass flow rate gradually increase
2 Continuous liquid-phase flow	0.0174- 0.152	Pressure, velocity, and mass flow rate decrease relatively smoothly
3 Interface transition	0.152- 0.161	Gas penetrates toward the nozzle; the velocity- mass flow rate relation begins to change
4 Intermittent joint outflow	0.161- 0.210	Mass flow rate and velocity fluctuate repeatedly; appreciable liquid outflow remains
5 High velocity with low mass flow rate	0.210- 0.217	Velocity peaks while mass flow rate remains low
6 Tail of the record	0.217- 0.23497	Overall decay; water and nonzero mass flow rate remain at the final recorded point

6.3 Phase-Dependent Changes in the Gas- Liquid Interface and Flow Field

The data curves show the overall changes, while the Fluent animations further reveal the spatial evolution of the gas- liquid interface. Figure 6-3 shows the interface at six times during discharge.

2026 S·T·Yau High School Science Award
仅用于2026丘成桐中学科学奖论文公示

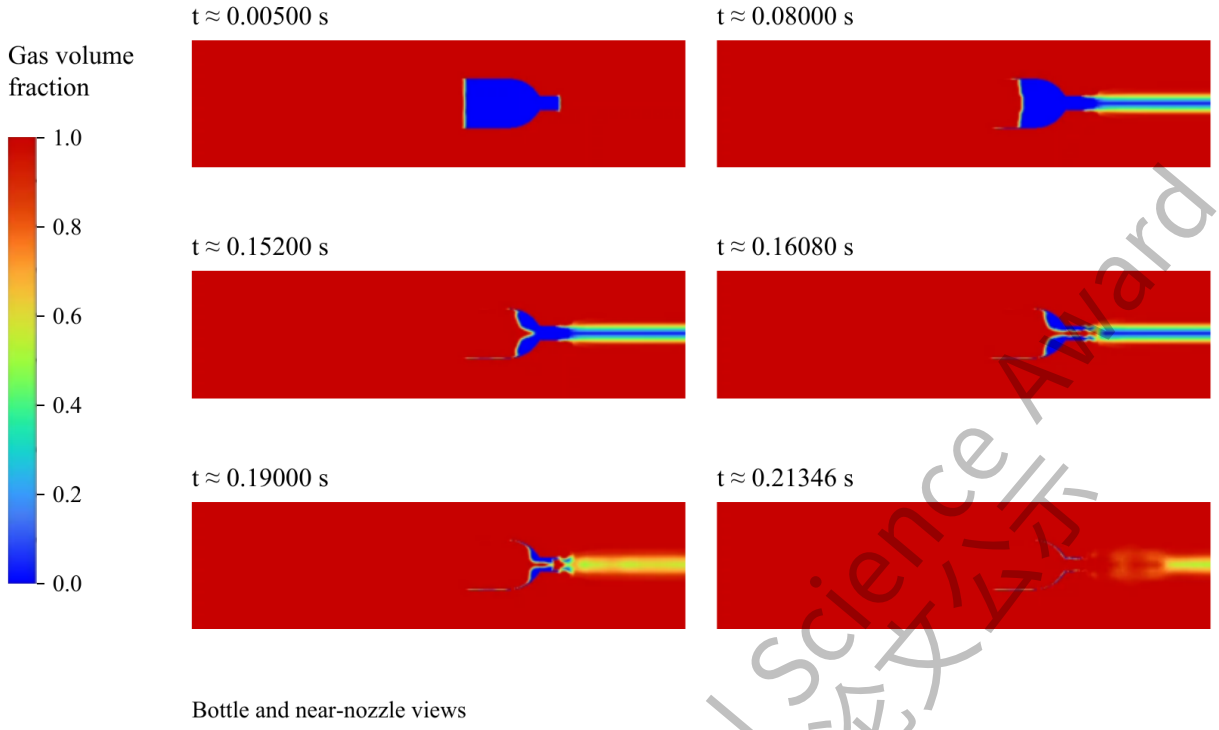


Figure 6-3. Key frames from the gas- liquid volume fraction video

The water volume decreases during discharge, and gas progressively approaches the outlet. Water remaining in the bottle does not necessarily mean that the nozzle is still filled with water. A model based only on remaining water volume cannot distinguish a water-filled outlet from one containing both gas and water. This is consistent with previous observations of gas entering the nozzle before all the water has left [10].

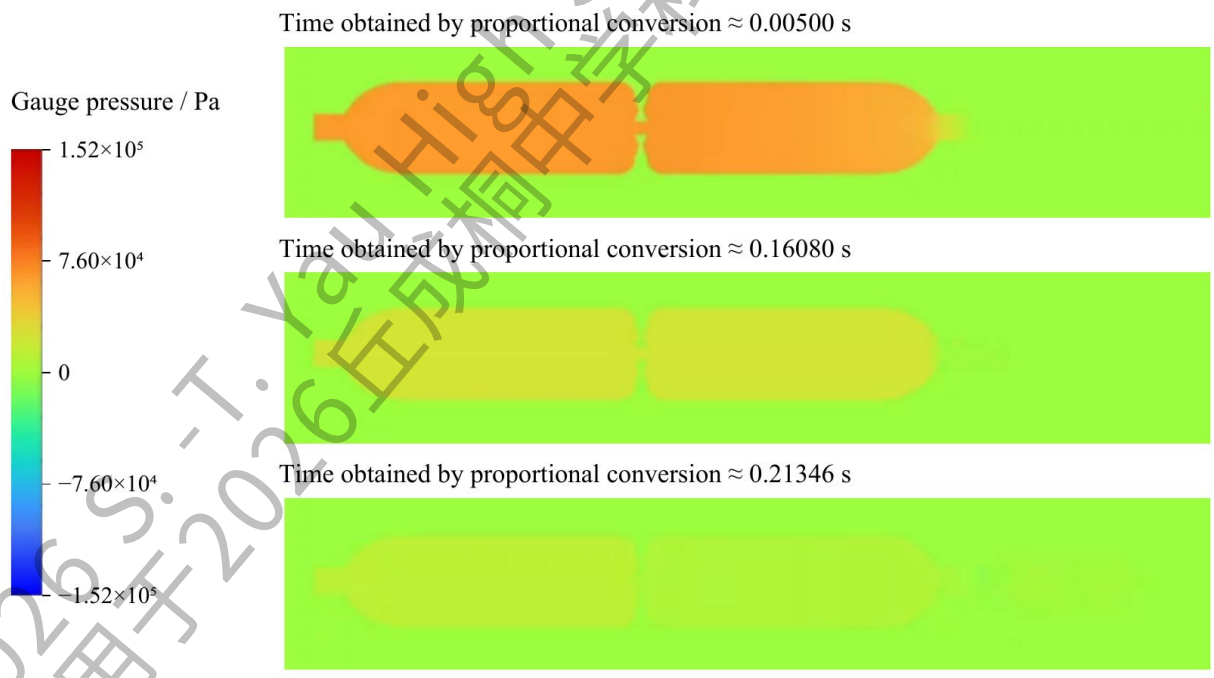


Figure 6-4. Key frames from the pressure video, in Pa. Pressure is not completely uniform in space

2026 S.-T. Yau High School Science Award
仅用于2026丘成桐中学科学奖论文公示

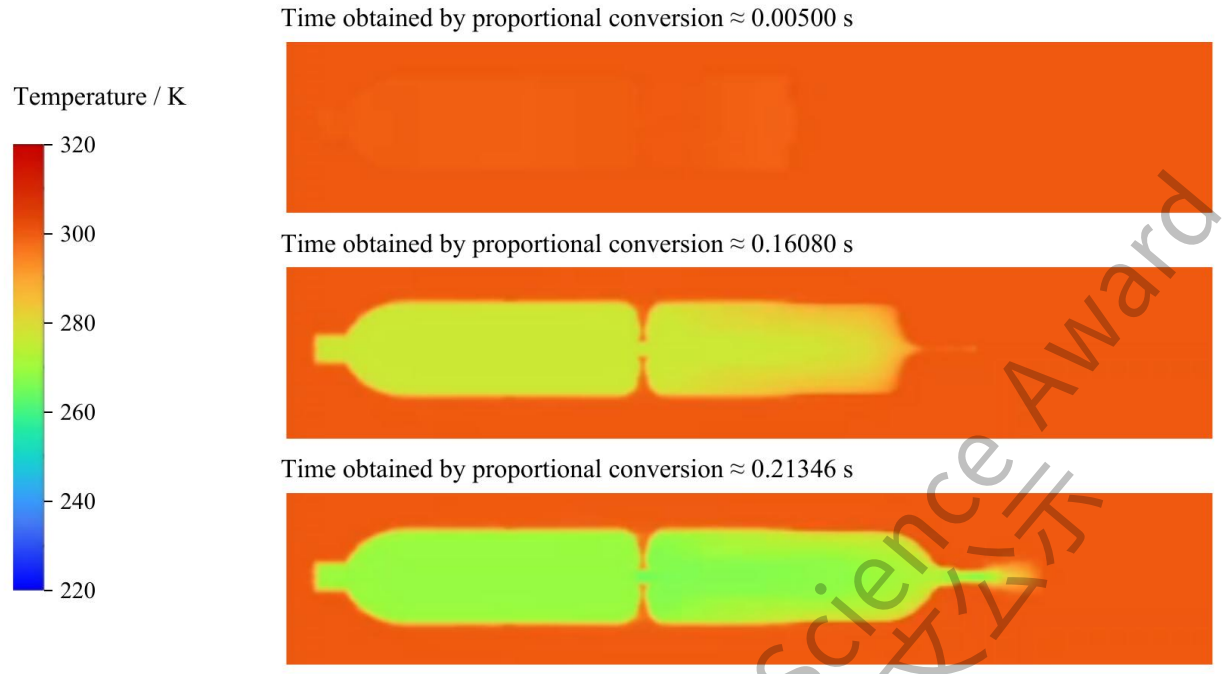


Figure 6-5. Key frames from the temperature video, in K

7 Corrections to the Formulas

7.1 Corrections for Liquid Inertia and Flow Losses During Startup

Near 0.001 s, the CFD pressure is approximately 59.76 kPa, while the velocity is only 1.35 m/s. Substituting the same pressure and prescribed head into Eq. (5-3) gives approximately 11.10 m/s, which is clearly too high. The liquid is still accelerating at this point, but the quasi-steady formula already treats the flow as developed.

This discrepancy points first to unsteady inertia, namely the pressure required to accelerate the liquid. We therefore add liquid-inertance and flow-loss terms to the Bernoulli pressure balance:

$$\Delta P + \rho_l g H \approx \frac{\rho_l}{2}(\beta_A + K)u^2 + I\frac{\mathrm{d}u}{\mathrm{d}t}. \tag{7-1}$$

Only two terms have been added to the original relation. $K\rho_l u^2/2$ represents all flow losses combined: the larger K is, the greater the pressure difference required for the same velocity. The term $I\,\mathrm{d}u/\mathrm{d}t$ represents liquid inertia and increases as the liquid accelerates more rapidly. Here, K is dimensionless and I has units of Pa·s^2/m. This unsteady pressure balance is consistent with the basic idea of liquid-inertia analysis [3, 5] ; the two coefficients are fitted to the CFD data here.

This relation calculates the required pressure difference from the known outlet velocity.

Differentiating a fluctuating velocity point by point can amplify noise. Time is therefore divided into short windows of 1 ms, and the mean pressure and velocity change are compared within each window:

$$\overline{\Delta P} + \rho_l g \overline{H} \approx \frac{\rho_l}{2}(\beta_A + K)\overline{u_r^2} + I\frac{u_r(t_b) - u_r(t_a)}{t_b - t_a}. \tag{7-2}$$

The overbar indicates an average over same time window.

A joint fit of Eq. (7-2) over 0- 0.152 s, using a liquid density of 1000 kg/m³, gives $K = 0.29012$ and $I = 49.205\ \mathrm{Pa\,s^2/m}$.

The CFD velocity changes from about 1.354 to 2.631 m/s between t = 1 ms and t = 2 ms, giving a mean rate of change of about 1278 m/s². The fitted inertial term is ~62.87 kPa and the velocity-square and loss terms are ~2.66 kPa. Subtracting the mean gravitational pressure contribution of 1.519 kPa gives a calculated pressure of

2026 S. T. Yau High School Science Award
应用于2026丘成桐中学科学奖公示

approximately 64.01 kPa, compared with the CFD window mean of 62.72 kPa. At start up, the liquid inertia is therefore still predominant.

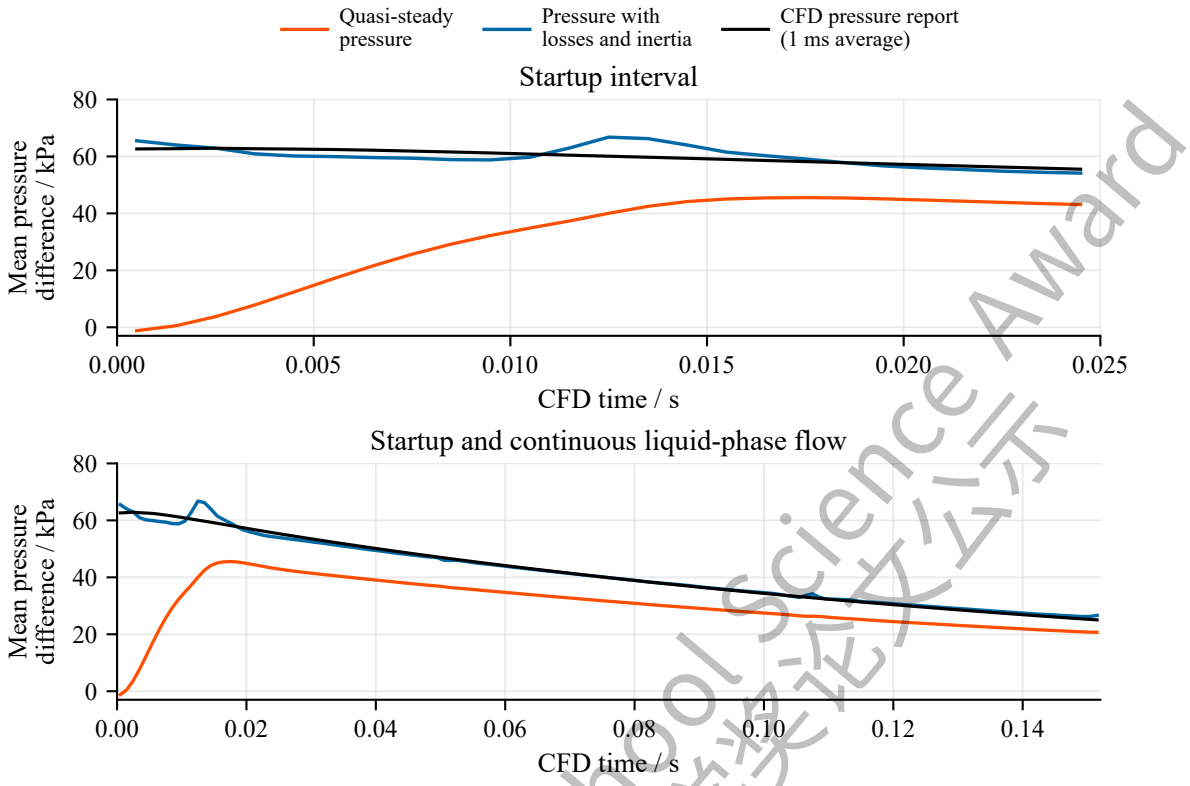


Figure 7-1. Comparison of the required pressure difference before and after adding inertia and losses. The upper panel enlarges the startup interval; the lower panel covers 0- 0.152 s

Table 7-1. RMSE of the required pressure difference over 1 ms windows after adding different terms, in kPa

Fitting interval	Quasi-steady baseline	Losses only	Inertia only	Both terms
Startup phase 1	39.39	32.69	7.681	2.938
Startup and liquid-phase flow, 1 + 2	15.42	11.78	9.551	1.211

The coefficients in each row of Table 7-1 are fitted over that row's interval, so the startup-only fit can differ from the fit over 0- 0.152 s. The main quasi-steady discrepancy occurs during startup, and losses alone do not describe the velocity buildup from rest. The pressure error for phases 1 + 2 decreases by about 92.1% when both of the terms are added.

Changing the averaging window from 0.5 to 4 ms changes the fitted I over phases 1 + 2 only from about 49.159 to 49.358, while K remains close to 0.29012. If the pure-liquid relation is used throughout the entire process it does not render the same improvement. The inertia correction is thus still valid for the early flow.

7.2 Coefficient Corrections for Velocity and Mass Flow Rate During Continuous Liquid-Phase Flow

7.2.1 Outlet Velocity Coefficient Correction

During 0.0174- 0.152 s, the velocity has developed and both pressure and velocity change relatively smoothly. In this interval, the original formula overpredicts velocity but captures its declining trend. We therefore retain the square-root relation and add only a velocity coefficient C_v:

$$u_{\mathrm{calc}} = C_v \sqrt{\frac{2[P_r + \rho_l g H]}{\rho_l \beta_A}}, \qquad C_v = 0.89234. \tag{7-3}$$

2026 S. T. YAU High School Science Award
仅用于2026丘成桐中学科学奖论文公示

The fitted coefficient may account for flow losses, contraction, and velocity averaging; their separate contributions have not been determined.

7.2.2 Mass Flow Rate Coefficient Correction

Even with CFD outlet velocity as the input, $q = \rho_l A u_r$ overpredicts the mass flow rate in this interval. We therefore introduce a separate mass flow rate coefficient C_q:

$$q_{\mathrm{calc}} = C_q \rho_l A u_r, \qquad C_q = 0.90487. \tag{7-4}$$

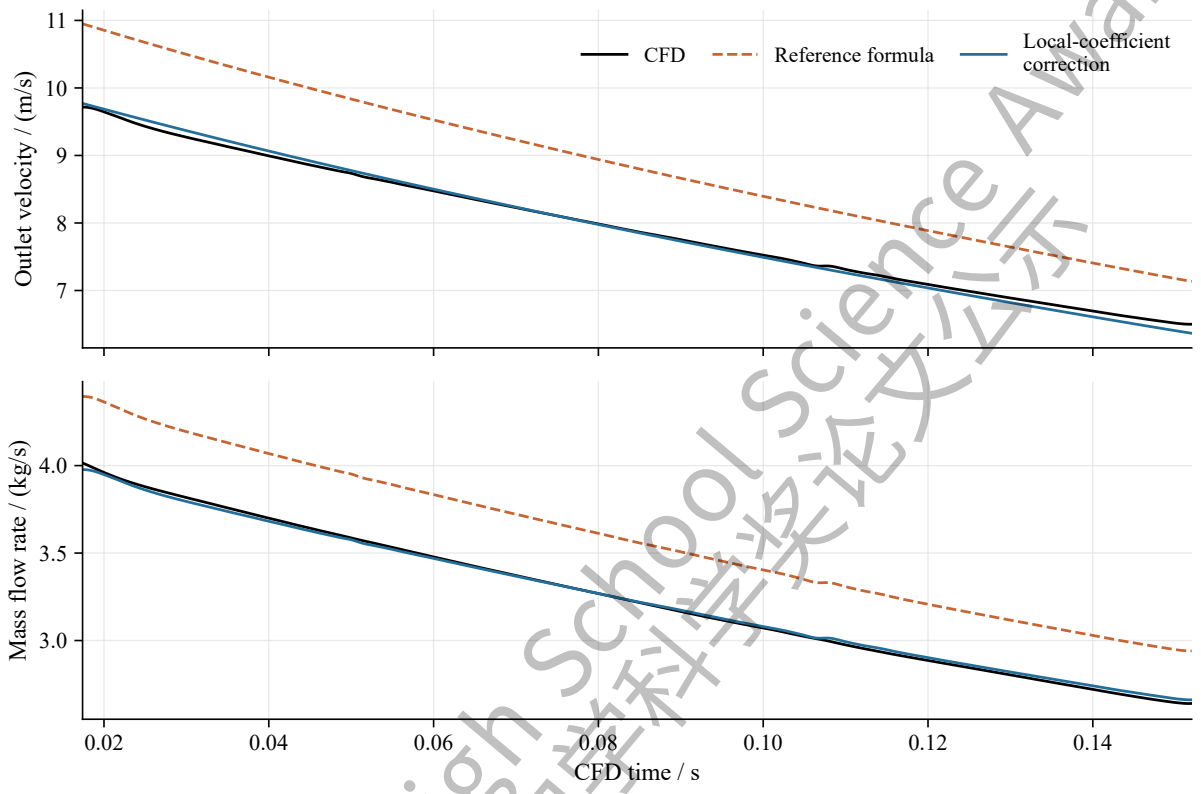


Figure 7-2. The upper panel calculates outlet velocity from CFD pressure and the prescribed head; the lower panel calculates mass flow rate from CFD outlet velocity

Table 7-2. Errors after separate corrections to velocity and mass flow rate

Quantity tested	Baseline RMSE	Corrected RMSE	Error reduction	Corrected R^2
Velocity / (m/s)	0.9656	0.05900	93.9%	0.99588
Mass flow rate / (kg/s)	0.3441	0.01485	95.7%	0.99855

Separate velocity and mass flow rate coefficients are therefore retained for this interval. Time-block resampling gives ranges of 0.89040- 0.89417 for C_v and 0.90366- 0.90605 for C_q, indicating relative stability within this part of the record.

7.3 Breakdown of the Pure-Liquid Approximation After the Gas- Liquid Transition

7.3.1 Testing Mass Flow Rate at Later Times

At the outlet-velocity peak (0.21346 s, phase 5), the CFD velocity is 33.522 m/s. The pure-liquid formula gives approximately 15.16 kg/s; applying the liquid-phase mass-flow coefficient reduces this to approximately 13.72 kg/s. The CFD mass flow rate is only 0.111 kg/s, more than two orders of magnitude below both estimates.

2026 S.T. Yau High School Science Award 仅用于2026年丘成桐中学科学奖论文公示

This difference indicates that the velocity- mass flow rate relationship becomes different in this phase and cannot be expressed with a certain proportional coefficient. The material flowing at high speed may be predominantly low-density gas, or the mean velocity may no longer represent the water carrying most of the mass. Treating the entire outlet area and the mean outlet velocity as uniform pure-water flow would significantly overestimate mass flow rate.

7.3.2 Differences in the Mass Flow Rate Coefficient Between Phases

To show this change, we rearrange Eq. (7-4) and calculate

$$C_{q,\mathrm{obs}}(t) = \frac{q_r(t)}{\rho_l A u_r(t)}. \tag{7-5}$$

The ratio compares the CFD mass flow rate q_r with the pure-water prediction $\rho_l A u_r$. If the original approximation of uniform pure-water flow holds, it should be close to 1. If one constant mass flow rate coefficient is sufficient, this ratio should remain approximately constant over the interval.

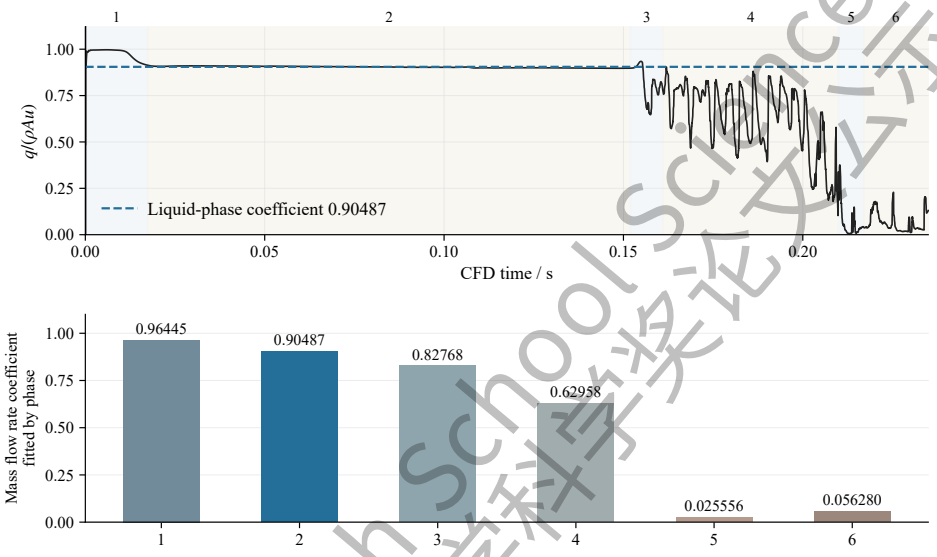


Figure 7-3. The upper panel shows the ratio of the CFD-reported mass flow rate to the value calculated from the pure-water relation, $q_r/(\rho_l A u_r)$; the lower panel shows the mass flow rate coefficients obtained separately for the six phases

The coefficient is approximately 0.90487 in phase 2, falls to approximately 0.62958 in phase 4, and is only approximately 0.025556 in phase 5. Clearly, C_q at later times is no longer the same constant as at early times.

7.3.3 Limitations of a Constant Effective Density

A single effective density was fitted and used in both the velocity and mass flow rate formulas, including the hydrostatic term. A combined fit gives approximately 582.59 kg/m^3, reducing the full-record mass flow rate RMSE from 1.321 to 0.7984 kg/s, but increasing the velocity RMSE from 2.922 to 4.411 m/s. Lowering density therefore still reduces the flux overprediction while increasing the calculated velocity and worsening its error.

Without additional coefficients, the velocity and mass flow rate relations give:

$$u^2 = \frac{2(\Delta P + \rho_{\mathrm{eff}} g H)}{\rho_{\mathrm{eff}} \beta_A}, \qquad qu = \rho_{\mathrm{eff}} A u^2 = \frac{2A(\Delta P + \rho_{\mathrm{eff}} g H)}{\beta_A}. \tag{7-6}$$

2026 Shi-Hua Cup High School Science Award
仅用于2026年度科学论文公示

Density cancels from the pressure-driven part of qu, but the gravitational contribution still depends on ρ_{eff}.

When the corrections in Eqs. (7-3) and (7-4) are used sequentially, the calculated velocity replaces u_r in the mass flow rate relation. With the same liquid density and liquid head in both relations, this gives

$$\begin{aligned} u_{\text{calc}} &= C_v \sqrt{\frac{2(\Delta P + \rho_l g H)}{\rho_l \beta_A}}, \\ q_{\text{calc}} &= C_q \rho_l A u_{\text{calc}}, \\ q_{\text{calc}} u_{\text{calc}} &= \frac{2AC_q C_v^2}{\beta_A}\Delta P + \frac{2AC_q C_v^2}{\beta_A}\rho_l g H. \end{aligned} \tag{7-6a}$$

Here, ΔP is the gauge pressure supplied to the velocity relation, either from CFD or from a pressure model. The coefficients $C_v = 0.89234$ and $C_q = 0.90487$ are obtained from liquid-phase fits. For fixed coefficients, the pressure-driven part of the calculated momentum term is independent of density, while the hydrostatic part still depends on density and liquid head. When the pressure term dominates, density-induced changes in velocity and mass flow rate can therefore cancel each other in their product.

7.4 Pressure Correction Accounting for Changes in Gas Mass

7.4.1 Effect of Adjusting the Expansion Exponent

The original pressure relation describes pressure reduction only through an increase in gas volume and assumes that the gas mass inside the bottle remains constant. We first try to replace the fixed value of the exponent 1.4 in Eq. (5-2) by an exponent n which can be fitted.

But it can be seen that taking n = 1 (isothermal approximation), will make the full record pressure RMSE worse (11.51 kPa). By only allowing n between 1- 1.4 in the fitting process, the resultant n value is very close to 1.4 with virtually no benefit. If this range is relaxed, the lowest error (3.837 kPa) is for the full record and occurs at about 1.4846, while the error at phase 2 increases from 1.043 to 1.634 kPa.

Fitting the exponent reduces the full-record pressure error but increases the phase 2 error, without explaining the cause of the late pressure decrease.

7.4.2 Gas-Loss Correction and Its Effect

After the gas- liquid transition, gas may leave through the outlet. Pressure then falls for two reasons: gas volume increases and gas mass inside the bottle decreases. For the simplified case of a uniform ideal gas undergoing approximately adiabatic discharge, the mass and energy relations give

$$\frac{P_g}{P_{g0}} = [\frac{m_g}{m_{g0}}\frac{V_{g0}}{V_g}]^{\gamma}. \tag{7-7}$$

Compared with the original formula, this adds only the gas mass ratio. When $m_g = m_{g0}$, Eq. (7-7) reduces to the original adiabatic formula; when gas mass decreases, it predicts a faster pressure decline.

The current CFD setup has no separate report for gas-phase mass outflow. During the study, the difference between total discharged mass and discharged water mass was therefore used to estimate gas mass loss:

$$B(t) = \int_0^t q_r(\tau)\,\mathrm{d}\tau - [m_{w,r}(0) - m_{w,r}(t)]. \tag{7-8}$$

This difference can reflect gas loss, but inconsistencies in report definitions and numerical errors may also introduce other contributions. We therefore do not directly treat $B(t)$ as the discharged gas mass, but introduce a fitted coefficient η to obtain the corrected expression

$$P_{\text{calc}} = P_{g0}[\frac{V_{g0}}{V_g(t)}\left(1 - \eta\frac{B(t)}{m_{g,\text{ref}}}\right)]^n - P_a. \tag{7-9}$$

Here, $m_{g,\text{ref}} = 0.00433659$ kg is the initial gas mass calculated with the initial gas temperature equal to the ambient temperature. Fixing $n = 1.4$ and fitting only η gives $\eta = 0.83406$.

2026 S. T. Yau High School Science Award
仅用于2026丘成桐中学科学奖公示

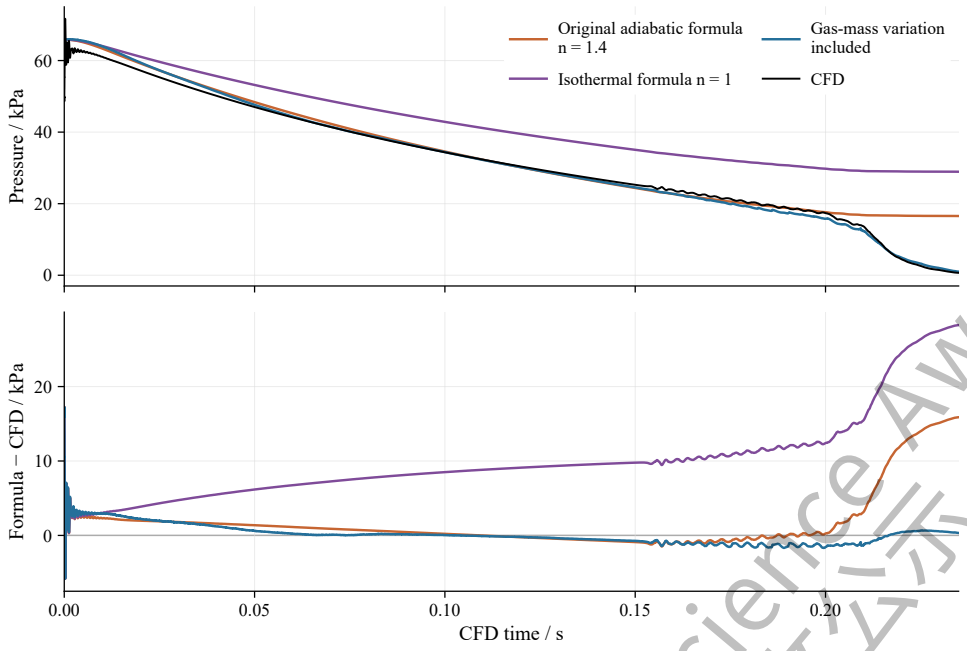


Figure 7-4. Comparison of pressure from the original adiabatic formula, the isothermal formula, and the gas-loss correction. The lower panel shows the formula result minus CFD

Table 7-3. Pressure-model modifications and resulting RMSE

Formula	Effective parameters	Full-record pressure RMSE / kPa	Phase 2 RMSE / kPa
Original adiabatic formula	Fixed $n = 1.4$	4.246	1.043
Isothermal formula	Fixed $n = 1$	11.51	7.737
Fitted exponent	$n = 1.4846$	3.837	1.634
Gas-loss term added	$n = 1.4$, $\eta = 0.83406$	1.248	0.8402
Gas-loss term and exponent fitted together	$n = 1.3788$, $\eta = 0.89353$	1.185	0.9265

Adding only the gas-loss term reduces the full-record pressure error by approximately 70.6%. Fitting the exponent as well reduces the error by only a further approximately 5.02%, while worsening the phase 2 error. We therefore keep the exponent at 1.4 and fit only the gas-loss coefficient.

7.5 Combined Corrections and Multivariable Tests During Liquid-Phase Flow

The preceding velocity test uses CFD pressure directly, while the mass flow rate test uses CFD velocity directly. We next combine the relations and jointly fit the velocity and mass flow rate coefficients over the continuous liquid-phase interval, checking pressure, velocity, mass flow rate, and remaining water mass against CFD. The formulas are:

$$\begin{aligned} V_g(t) &= V_b - \frac{m_{w,r}(t)}{\rho_l}, \\ P_{\mathrm{calc}}(t) &= P_{g0}\left[\frac{V_{g0}}{V_g(t)}\right]^{1.4} - P_a, \\ u_{\mathrm{calc}}(t) &= 0.88017\sqrt{\frac{2[P_{\mathrm{calc}} + \rho_l g H]}{\rho_l \beta_A}}, \\ q_{\mathrm{calc}}(t) &= 0.90969\rho_l A u_{\mathrm{calc}}(t). \end{aligned} \tag{7-10}$$

2026 S. T. Yau High School Science Award
仅用于2026丘成桐中学科学奖论文公示

The water-mass check starts at $t_s = 0.0174$ s with the CFD water mass of 0.5702026 kg. The calculated remaining mass, $m_{w,\mathrm{check}}(t)$, is obtained by subtracting the integral of q_{calc} from this initial value, following the mass balance in Eq. (5-4).

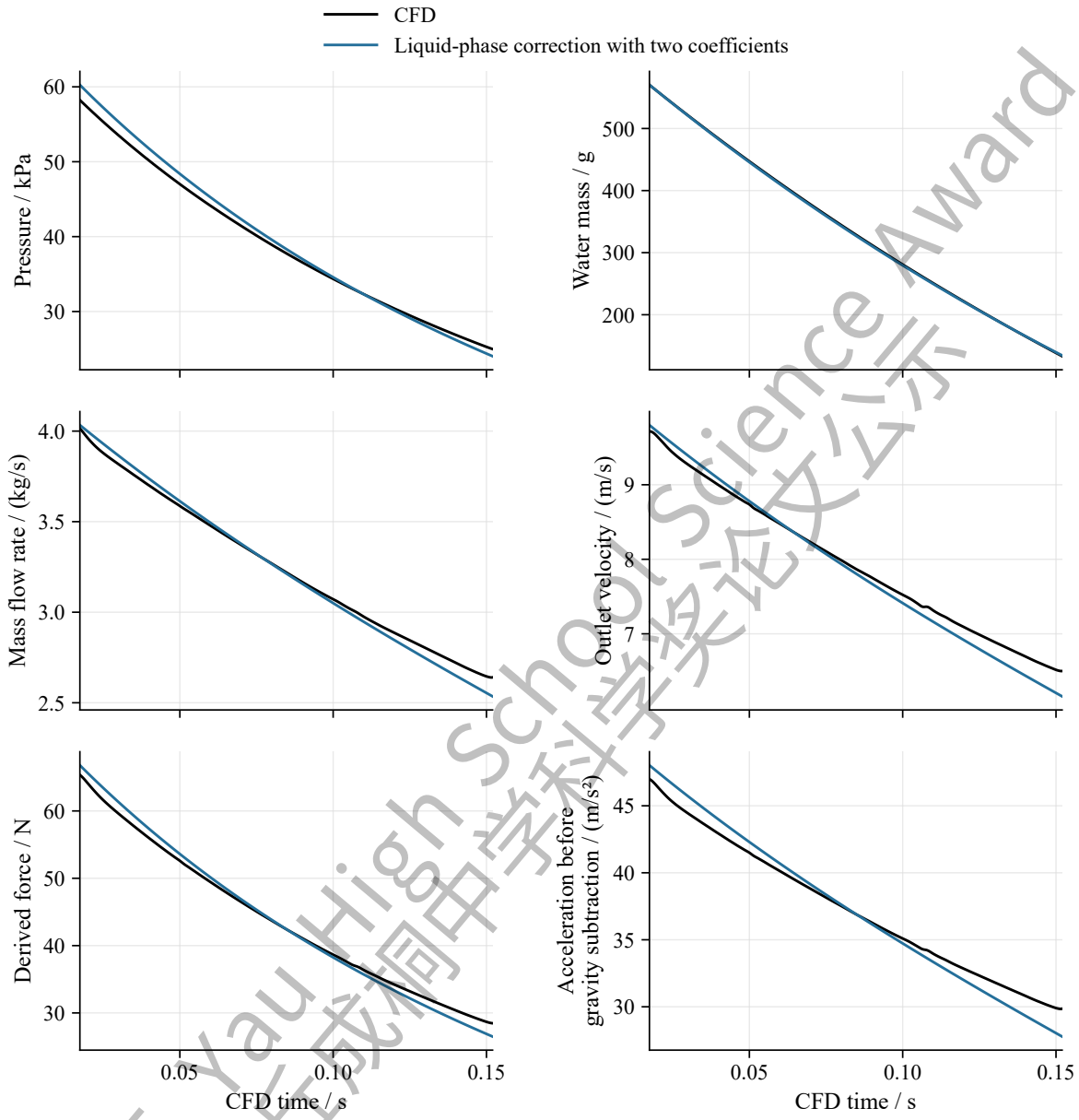


Figure 7-5. Comparison of the liquid-phase correction with two coefficients against CFD during continuous liquid-phase flow in Case A. Acceleration is shown before gravity subtraction

Table 7-4. Results of the liquid-phase correction with two coefficients over 0.0174- 0.152 s. Errors compare calculated values with CFD; acceleration is evaluated before gravity subtraction

Variable	RMSE	R^2
Pressure	1.043 kPa	0.98788
Velocity	0.1445 m/s	0.97526
Mass flow rate	0.04105 kg/s	0.98895
Water mass	1.167 g	0.99991
Derived force	1.078 N	0.98934
Acceleration F/M	0.9464 m/s^2	0.96205

2026 C. T. Yau High School Science Award
仅用于2026丘成桐中学科学奖论文公示

The combined correction gives 134.479 g of water at the end of phase 2, versus 133.199 g in CFD (difference 1.280 g). Its mass flow integral is 0.294% lower and its $\int F_{\mathrm{calc}}\,\mathrm{d}t$ is 0.104% higher than $\int F_r\,\mathrm{d}t$. These results use the CFD water mass to calculate pressure and H.

7.6 Applicability of Constant-Coefficient Combinations Over the Full Process

In this study this combination of the three (pressure exponent, velocity coefficient and mass flow rate coefficient) were also attempted for the entire process. For the full-record correction without the water-quantity constraint, the values of n, C_v and C_q were equal to 1.5420, 0.91365 and 0.83692, respectively. However, if the calculated mass flow rate is integrated to the last point recorded, the remaining water mass is -6.110 g which is unacceptable.

The fit was then run again with the water-quantity constraint which requires that the overall discharged water quantity does not exceed the initial water quantity, resulting in a full-record correction with water-quantity constraint. Its parameters are n=1.5474, C_v=0.91855, and C_q=0.82609. Although negative water mass no longer occurs, the final water mass is approximately zero, whereas CFD still contains 14.777 g. The late velocity peak also remains unexplained.

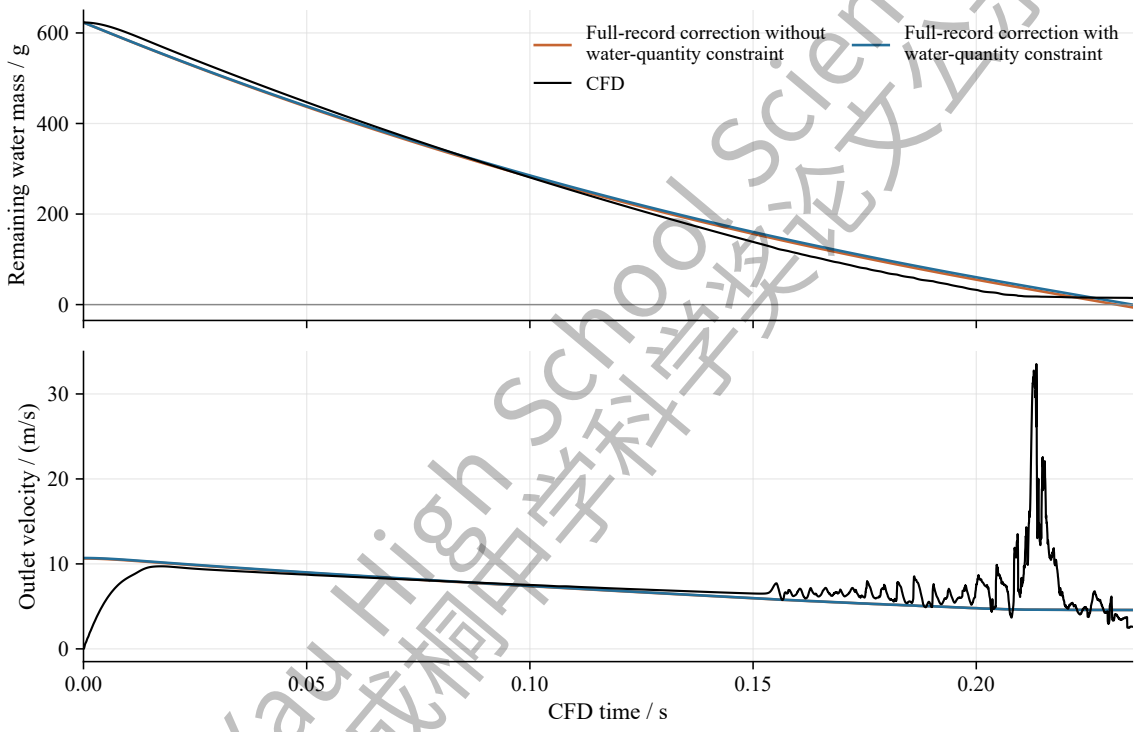


Figure 7-6. Comparison of two full-record constant-coefficient correction combinations with CFD

Table 7-5. Errors of the combined correction with a water-quantity constraint, relative to CFD. Acceleration is evaluated before gravity subtraction

Full-record variable	Baseline RMSE	Full-record correction with water-quantity constraint RMSE	Change
Pressure / kPa	4.246	4.061	Decrease of 4.35%
Water mass / g	135.7	16.67	Decrease of 87.7%
Mass flow rate / (kg/s)	1.321	0.7435	Decrease of 43.7%
Velocity / (m/s)	2.922	2.942	Increase of 0.693%
Derived force / N	15.57	8.448	Decrease of 45.8%
Acceleration F/M / (m/s^2)	13.40	7.646	Decrease of 42.9%

2026 S. T. Yau High School Science Award
仅用于2026丘成桐中学科学奖论文公示

The fitted constants describe the early liquid-phase flow but do not capture the later changes in outlet phase composition and velocity distribution. In the full-record fit, reductions in other errors are accompanied by a larger velocity error.

8 Effects of Rocket-Acceleration Feedback on Discharge

Sections 5- 7 examined the simplified relations using the baseline simulation without rocket-acceleration feedback. This section examines the case with rocket-acceleration feedback, first by comparing the six reported quantities and CFD images, and then by applying the same phase-identification criteria. The coefficients from the preceding section are retained in these tests.

8.1 Comparison of CFD Variables

Figure 8-1 compares the six reported quantities on their original time axes, using the same kinematic acceleration definition in both cases.

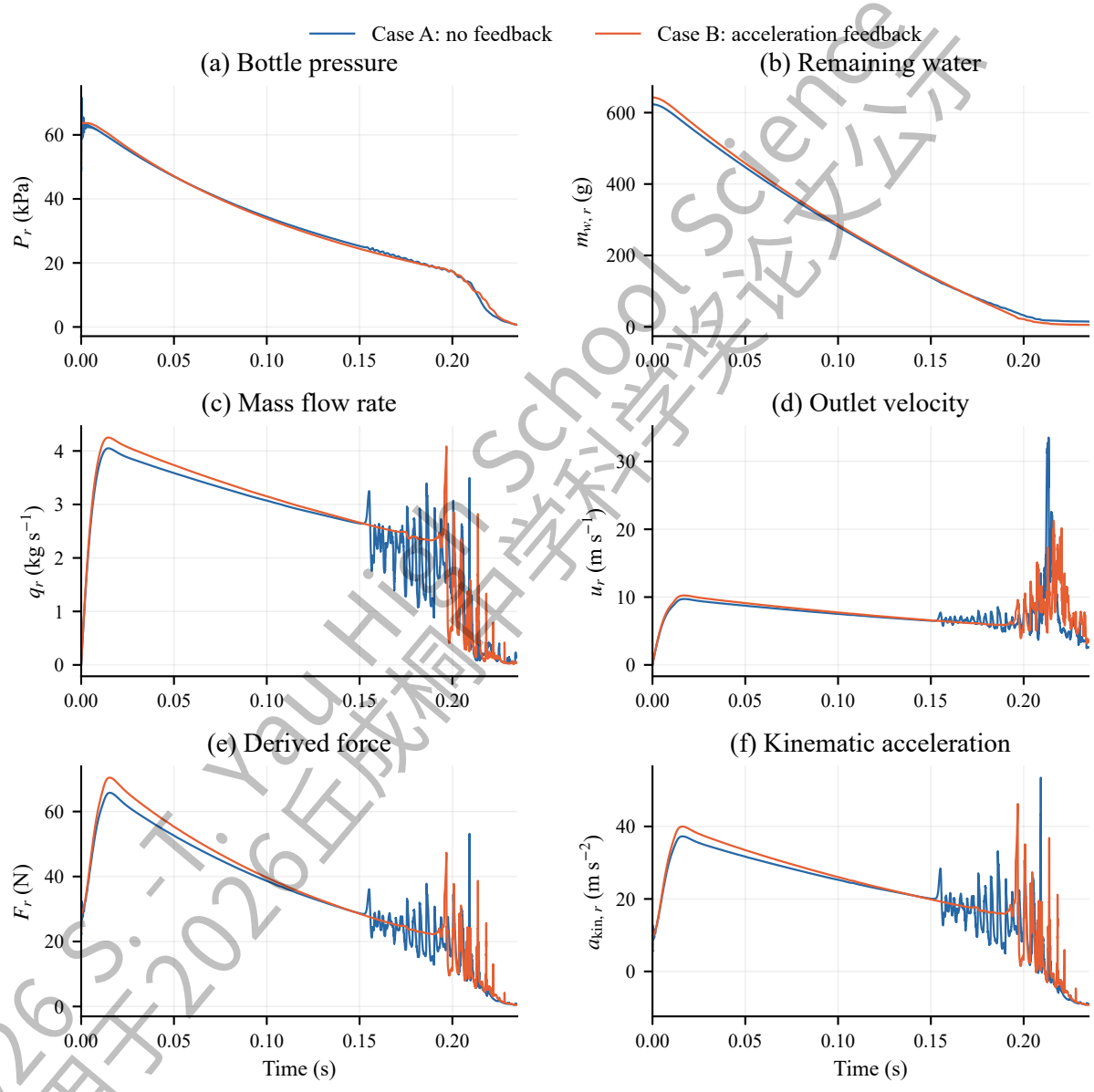


Figure 8-1. Comparison of the six reported quantities in Cases A and B: bottle gauge pressure, remaining water mass, outlet mass flow rate, area-weighted axial outlet velocity, derived thrust, and kinematic acceleration $a_{\mathrm{kin,r}}$. The original curves are shown without smoothing, and gravity is accounted for consistently in the acceleration.

2026 S. -T. Yau High School Science Award 仅用于2026丘成桐中学科学奖论文公开

During the common continuous liquid-phase flow interval of 0.03- 0.14 s, the pressure curves are close and the velocity, mass flow rate, thrust, and acceleration in Case B are slightly higher. Table 8-1 gives time-averaged values over this interval. The differences in these quantities remain within approximately 4%.

Table 8-1. Time-averaged quantities over 0.03- 0.14 s. The relative change is calculated as $(B - A)/A$.

Quantity	Case A	Case B	Change
Bottle gauge pressure / kPa	38.531	38.234	−0.773%
Remaining water mass / g	333.10	340.54	+2.23%
Outlet mass flow rate / (kg/s)	3.2338	3.3360	+3.16%
Mean axial outlet velocity / (m/s)	7.9041	8.1697	+3.36%
Derived thrust / N	43.228	44.856	+3.77%
Kinematic acceleration / (m/s^2)	27.313	28.407	+4.01%

There are larger variations in curve shape for the later curves. A large scale outlet fluctuation occurs sooner in Case A and a longer duration of gradual decay of the outlet velocity occurs in Case B, before the large scale outlet fluctuation set in. The maximum recorded outlet velocity is 33.522 m/s in Case A and 21.256 m/s in Case B. The maximum kinematic acceleration is 53.462 m/s² in Case A and 46.219 m/s² in Case B.

But the full-record thrust integrals of Cases A and B are 8.1875 N s and 8.5344 N s respectively, a difference of ~ 4.24%. The relative change in the thrust integral is therefore smaller than those in the late peak outlet velocity and acceleration.

8.2 Interface Evolution and Interpretation of the Changes

Figure 8-2 compares CFD gas-volume-fraction contours at matched remaining-water fractions. At a remaining-water fraction of 0.25, both cases retain a continuous liquid region near the nozzle. At a fraction of 0.15, Case A already has a pronounced central gas passage, while Case B retains a continuous liquid core. At fractions of 0.10 and 0.05, central gas intrusion and subsequent gas passages are also visible in Case B. The feedback therefore delays and changes the development of the gas passage.

The effective acceleration in the nozzle direction is, $b(t) = g + a(t)$, not just g. This, in turn, causes the body-force head during the upward acceleration of the rocket to be increased, and is included here as the pressure contribution across the liquid column, as shown by the following expression: $\rho_l bH$. The pressure difference caused by the body forces corresponding to an axial separation (δh) is of order ($\rho_l b\, \delta h$) [3, 17] . The stronger body force is associated with the longer persistence of the continuous liquid region and the delay in transitioning out of liquid-dominated discharge witnessed in Case B.

A nonuniform flow in the vicinity of the contracting outlet could still enable the passage of gas through the centre even if there is a decrease in the thickness of the liquid layer. As the gas passage widens the water filled outlet area and distributions of velocity and density in the local area will vary. The mean outlet velocity can then increase without a proportional increase in mass flow rate. Thus, pressure might drop (relatively) fairly smoothly, but velocity, flow rate, and acceleration might have large oscillations. These fluctuations are associated with the evolution of the gas passages shown in the CFD images.

2026 S. - Tianqi High School Science Award
仅用于2026年天启高中科学奖论文公示

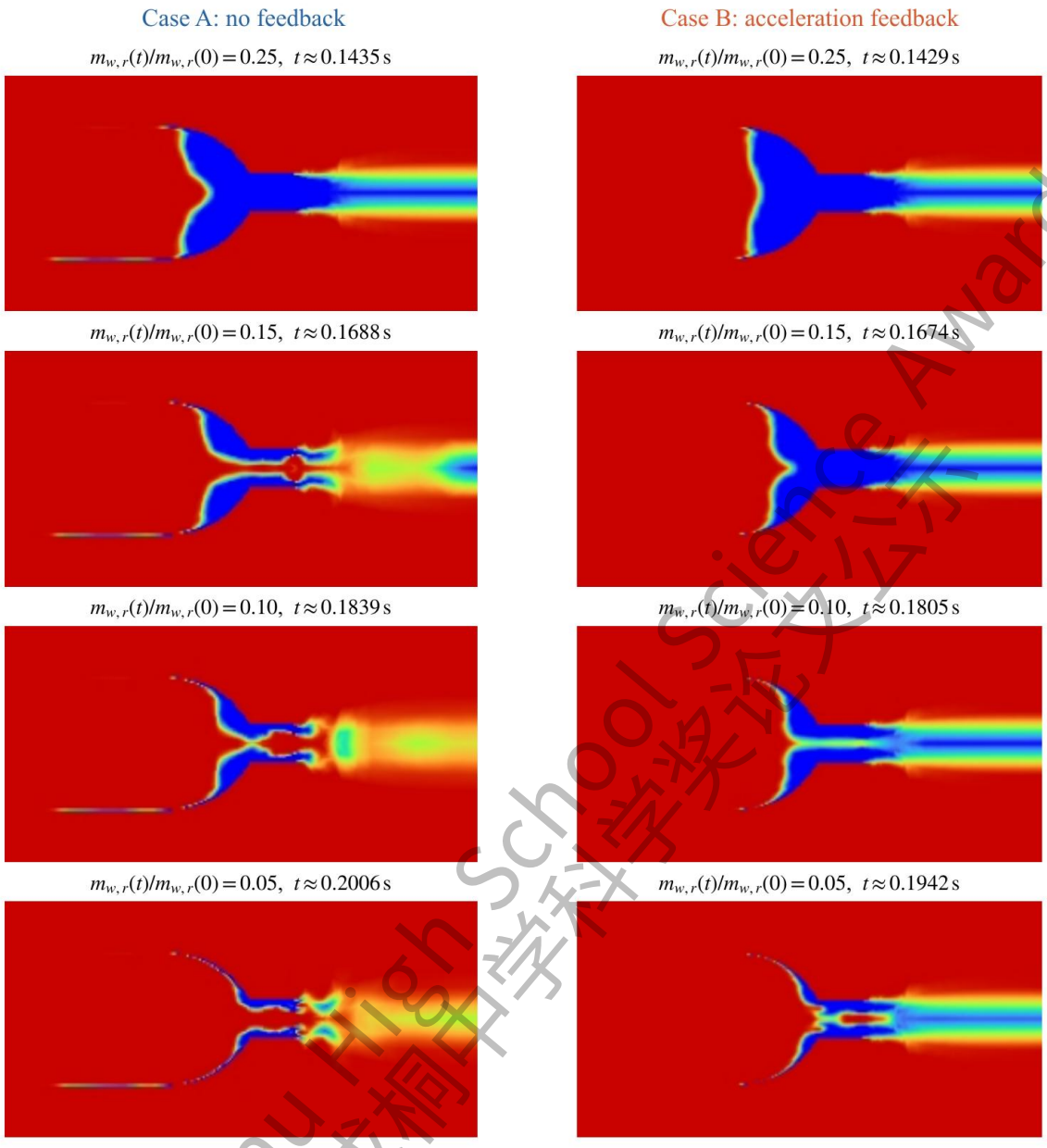


Figure 8-2. Gas- liquid interface evolution at matched remaining-water fractions in Cases A and B. Red denotes gas and blue denotes water.

8.3 Division into Flow Phases

Sections 6 and 7 retain the original analysis and parameter-fitting intervals. To compare the two cases, this section identifies the flow phases using the same quantitative criteria. Subsequent evaluations use the intervals identified for each case, while the original fitted coefficients remain unchanged. For identification only, the velocity and mass flow rate are interpolated at 10 μs intervals and smoothed using a third-order Savitzky-Golay filter [18] with 101 points, spanning 1 ms. The smoothed results are denoted by $\tilde{u}_r$ and $\tilde{q}_r$.

2026 S.-T. Yau High School Science Award
仅用于2026丘成桐中学科学奖公示

Let t_1 be the first main velocity peak, with a prominence of at least 0.5 m/s, and define $U_L = \tilde{u}_r(t_1)$. Let t_2 be the first subsequent velocity minimum with a prominence of at least $0.05U_L$. A measure of departure from the liquid mass-flow relation is then defined as

$$R(t) = \frac{\tilde{q}_r(t)}{\rho_l A \tilde{u}_r(t)}, \qquad \chi(t) = \frac{R(t)}{R_L}, \tag{8-1}$$

where R_L is the median of R over the central 80% of $[t_1, t_2]$. The values of U_L are 9.7161 and 10.243 m/s, and the values of R_L are 0.90426 and 0.90098, for Cases A and B, respectively.

After t_2, t_3 is the first time at which $\chi < 0.90$ persists for at least 0.5 ms. After t_3, t_4 is the first time at which both $\chi < 0.20$ and $\tilde{u}_r > U_L$ persist for at least 0.5 ms. Finally, after the largest smoothed velocity peak following t_4, t_5 is the first time at which $\tilde{u}_r < U_L$ persists for at least 0.5 ms. The last interval ends at the end of the simulation. Figure 8-3 and Table 8-2 show the resulting division.

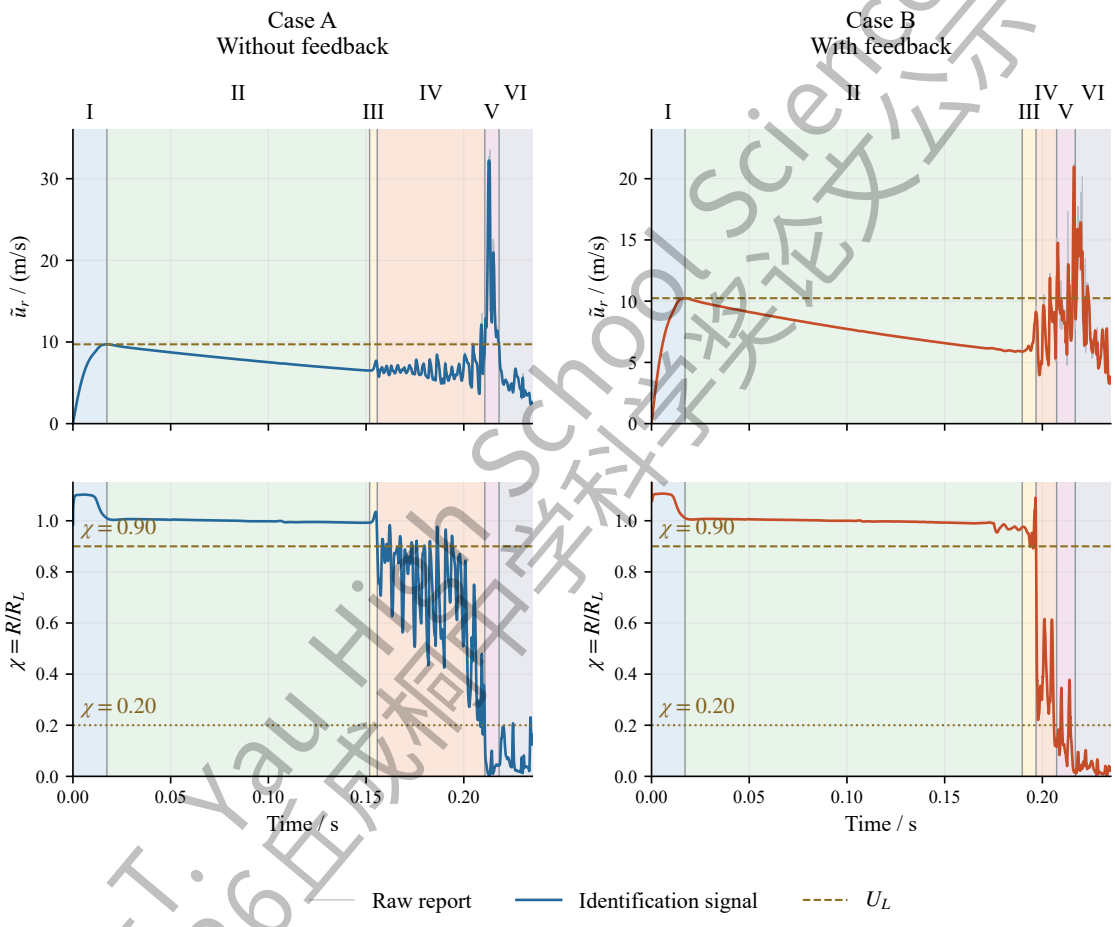


Figure 8-3. Six-phase identification using the same velocity and normalized mass-flow criteria in both cases. Grey curves show the raw reports; coloured curves show the identification indicators. Shaded intervals indicate phases I- VI.

2026 S.-T. Yau High School Science Award
仅用于2026丘成桐中学科学奖论文公示

Table 8-2. Phase intervals obtained using the common identification criteria.

Phase	Main characteristic	Case A / s	Case B / s
I	Startup and velocity buildup	0- 0.01738	0- 0.01713
II	Continuous liquid-dominated discharge	0.01738- 0.15180	0.01713- 0.18971
III	Transition in the outlet response	0.15180- 0.15575	0.18971- 0.19678
IV	Intermittent outflow with marked departure from the liquid relation	0.15575- 0.21076	0.19678- 0.20731
V	High velocity with low mass flow rate	0.21076- 0.21805	0.20731- 0.21685
VI	Decay and fluctuations in the recorded tail	0.21805- 0.23497	0.21685- 0.23498

The startup duration changes little. Phase II lengthens from 134.42 to 172.58 ms, whereas phase IV shortens from 55.01 to 10.53 ms. At t_3, the remaining-water fraction is approximately 19.66% in Case A but only 3.815% in Case B. The sustained departure from the liquid mass-flow relation therefore occurs after a much larger fraction of the water has left in Case B. The combined contribution of phases I and II to the full-record thrust integral increases from 82.95% to 94.00%.

8.4 Applicability of the Original Corrections

All coefficients in this section retain their fitted values from Case A. With $M_r(t) = m_{\text{fixed}} + m_{w,r}(t)$, the calculated kinematic acceleration is

$$a_{\text{kin,calc}} = \frac{F_{\text{calc}}}{M_r} - g.$$

The body-force acceleration used in the flow relation is

$$b = \begin{cases} g, & \text{Case A,} \\ g + a_{\text{kin,calc}} = F_{\text{calc}}/M_r, & \text{Case B.} \end{cases}$$

In Case B, $b = g_{\text{eff}}$.

The CFD remaining water mass is retained in M_r, and the column height follows the same assumption of a linear decrease with remaining water mass. In Case B, the predicted acceleration is solved together with the flow relation and fed back into the head. The CFD inputs retained in each test are stated in the following subsections.

8.4.1 Startup Inertia and Flow Losses

For the startup pressure test, the balance becomes

$$P_{\text{calc}} + \rho_l b H \approx \frac{\rho_l}{2}(\beta_A + K)u_r^2 + I\frac{\mathrm{d}u_r}{\mathrm{d}t}, \qquad K = 0.29012, \quad I = 49.205\ \text{Pa s}^2/\text{m}. \tag{8-2}$$

Here, the fluid inertance term $I\,\mathrm{d}u_r/\mathrm{d}t$ [5] describes the pressure difference required to establish the relative outflow. The pressure test uses q_r and u_r from CFD and, with the outlet-pressure approximation in Section 5.2, evaluates $b = (q_r u_r + A_e P_{\text{calc}})/M_r$. Representing the calculated pressure by a constant P_w within each 1 ms window and averaging Eq. (8-2) gives

$$P_w = \frac{\frac{\rho_l}{2}(\beta_A + K)\overline{u_r^2} + I\frac{\Delta u_r}{\Delta t} - \rho_l\frac{\overline{H q_r u_r}}{M_r}}{1 + \rho_l A_e\frac{\overline{H}}{M_r}}. \tag{8-2a}$$

2026 S. - T. Yau High School Science Award
仅用于2026丘成桐中学科学奖论文公示

The overbar denotes the mean within the window. Setting $I = 0$, $K = 0$, or both to zero gives the loss-only, inertance-only, and original relations, respectively. Table 8-3 compares P_w with the corresponding CFD window mean.

Table 8-3. Pressure RMSE in Case B over complete 1 ms windows, in kPa, with acceleration calculated from each tested relation and fed back into the head. The listed intervals are the actual window coverage within phases I and I-II.

Interval	Original	Loss only	Inertance only	Both
Startup: 0-0.017 s	39.80	35.18	9.128	3.396
Phases I-II: 0-0.189 s	13.97	10.71	8.863	1.508

The combined correction reduces startup pressure error by 91.47%, whereas adding losses alone reduces it by only 11.60%. During 1-2 ms, the liquid-inertance contribution is approximately 65.49 kPa, compared with 2.917 kPa for the velocity-squared and loss terms and 3.413 kPa for the body-force head in the combined correction. The original conclusion that liquid inertia dominates startup therefore remains applicable when rocket-acceleration feedback is included.

8.4.2 Liquid-Phase Velocity and Mass Flow Rate Coefficients

The velocity and mass flow rate relations are tested separately using Eqs. (7-3) and (7-4), retaining $C_v = 0.89234$ and $C_q = 0.90487$ and replacing gH with bH in the velocity relation.

In the Case B velocity test, P_r and q_r are retained from CFD, and $b = (q_r u_{\mathrm{calc}} + A_e P_r)/M_r$ is solved together with the velocity relation; Case A uses $b = g$. The mass flow rate test retains u_r and does not contain a body-force head. Table 8-4 tests these formulas over phase II identified separately in each case. Both coefficients reduce the corresponding RMSE over the longer Case B phase II, although the corrected RMSE values remain slightly higher than in Case A.

Table 8-4. RMSE for the velocity and mass flow rate relations before and after applying the original coefficients over each case's phase II.

Case	Quantity	Original	Corrected	Reduction
A	Velocity / (m/s)	0.9660	0.05882	93.91%
A	Mass flow rate / (kg/s)	0.3442	0.01484	95.69%
B	Velocity / (m/s)	0.8930	0.1521	82.97%
B	Mass flow rate / (kg/s)	0.3539	0.03036	91.42%

8.4.3 Constant Effective Density

The effective density of 582.59 kg/m³ is also tested in both the velocity and mass flow rate formulas, including the body-force head. It decreases the full-record mass flow rate RMSE from 1.275 to 0.7826 kg/s in Case B, while the velocity RMSE increases from 2.564 to 4.021 m/s. Hence, the same conflict exists as in Case A: On a lower density the calculated mass flow rate gets lower, the calculated velocity higher. A single constant effective density is still not suitable for representing the evolving two-phase outlet over the full process.

8.4.4 Gas-Mass-Loss Pressure Correction

Equation (7-9) is evaluated using the Case B gas-volume history and mass difference $B(t)$ defined in Eq. (7-8), while retaining the original coefficients. With $n = 1.4$ and $\eta = 0.83406$, the full-record pressure RMSE falls from 3.382 to 1.151 kPa. The alternative original pair, $n = 1.3788$ and $\eta = 0.89353$, gives 1.051 kPa. By comparison, using the original exponent-only fit $n = 1.4846$ gives 3.592 kPa, which is slightly worse than the

2026 Siyuan High School Science Award
仅用于2026思源中学科学奖公示

uncorrected expansion relation in this case. Thus, accounting for gas loss remains effective, while the benefit of changing only the closed-system expansion exponent does not transfer to Case B.

8.4.5 Combined Corrections Fitted to the Liquid-Phase Interval or the Full Record

The local liquid-phase combination of Eq. (7-10) retains C_v=0.88017, C_q=0.90969, and the exponent 1.4. These are the jointly fitted local coefficients, rather than the two independently fitted coefficients in Eqs. (7-3) and (7-4). The mass check is performed starting from the CFD water mass at t_1 and adds up the calculated mass flow rate for each new phase II identified. For Case B, the end-of-phase water mass is overpredicted by 15.41 g whereas for Case A it is 1.259 g for the same procedure for phase identification. The mass flow integral value for the Case B is 2.827% lower than the CFD, whilst the thrust integral value for the Case B is 4.176% lower than the CFD. The errors for the combination are also as follows: End of the phase water-mass error is larger and also the mass flow and thrust integral errors are larger over the longer Case B interval.

The two full-record constant-coefficient combinations of Section 7.6 also retain their original parameters. In Case B, they predict final water masses of 16.18 and 22.45 g, respectively, compared with 5.705 g in CFD. Their velocity RMSE values are 2.645 and 2.653 m/s, respectively, both higher than the baseline value of 2.564 m/s. These two transferred combinations therefore still fail to reproduce both the remaining water mass and outlet velocity in Case B.

8.4.6 Acceleration Calculated Using the Combined Corrections

Figure 8-4 summarizes the original corrections applied to Case B. For the combined acceleration curve, Eq. (7-9) supplies pressure with $n = 1.4$ and $\eta = 0.83406$. The startup velocity is calculated from the differential pressure balance with the original I and K, starting from zero velocity. During this startup branch, $q_{\mathrm{calc}} = \rho_l A u_{\mathrm{calc}}$, and the head uses $b = (\rho_l A u_{\mathrm{calc}}^2 + A_e P_{\mathrm{calc}})/M_r$ at each integration step. The switch to $C_v = 0.89234$ and $C_q = 0.90487$ occurs at 0.0174 s, after which those coefficients are used through the remaining record. The post-startup relations are solved simultaneously:

$$u_{\mathrm{calc}} = C_v \sqrt{\frac{2(P_{\mathrm{calc}} + \rho_l b H)}{\rho_l \beta_A}}, \quad q_{\mathrm{calc}} = C_q \rho_l A u_{\mathrm{calc}},$$

$$F_{\mathrm{calc}} = q_{\mathrm{calc}} u_{\mathrm{calc}} + A_e P_{\mathrm{calc}}, \qquad b = \frac{F_{\mathrm{calc}}}{M_r}.$$

The kinematic acceleration is $a_{\mathrm{kin,calc}} = b - g$. The calculation retains the CFD remaining water mass and the thrust definition used in the paper. The original formulas also calculate acceleration and feed it back into the flow relation, using the original expansion pressure and $C_v = C_q = 1$. In Figure 8-4(a), the startup differential equation instead uses P_r from CFD, with acceleration calculated from that branch's own velocity and mass flow rate.

The full-record acceleration RMSE falls from 12.94 to 3.303 m/s^2, a reduction of approximately 74.47%. After the startup branch, the product of velocity and mass flow rate satisfies

$$q_{\mathrm{calc}} u_{\mathrm{calc}} = k(P_{\mathrm{calc}} + \rho_l b H), \qquad k = \frac{2 A C_q C_v^2}{\beta_A}. \tag{8-3}$$

Substituting $b = (q_{\mathrm{calc}} u_{\mathrm{calc}} + A_e P_{\mathrm{calc}})/M_r$ gives

$$q_{\mathrm{calc}} u_{\mathrm{calc}} = \frac{k P_{\mathrm{calc}} (1 + \rho_l A_e H / M_r)}{1 - k \rho_l H / M_r}. \tag{8-3a}$$

Although the explicit density factors cancel out of the pressure term in Eq. (8-3), a density dependence does appear in the acceleration feedback term, which depends on $\rho_l H/M_r$ [see, e.g., Eq. (8-3a)]. When both the dimensionless ratio $\rho_l A_e H/M_r$ and the dimensionless ratio $k\rho_l H/M_r$ are small, the momentum-flux product is

2026 S. T. Yau High School Science Award
仅用于2026丘成桐科学奖公示

~kP_{calc}. This cancelation is the reason why the reduction of pressure error could cause calculated thrust and acceleration errors to be reduced even if the outlet velocity and the mass flow rate are wrong. The combination, however, does not give a physically consistent description of the entire process since the calculated water mass still differs from CFD.

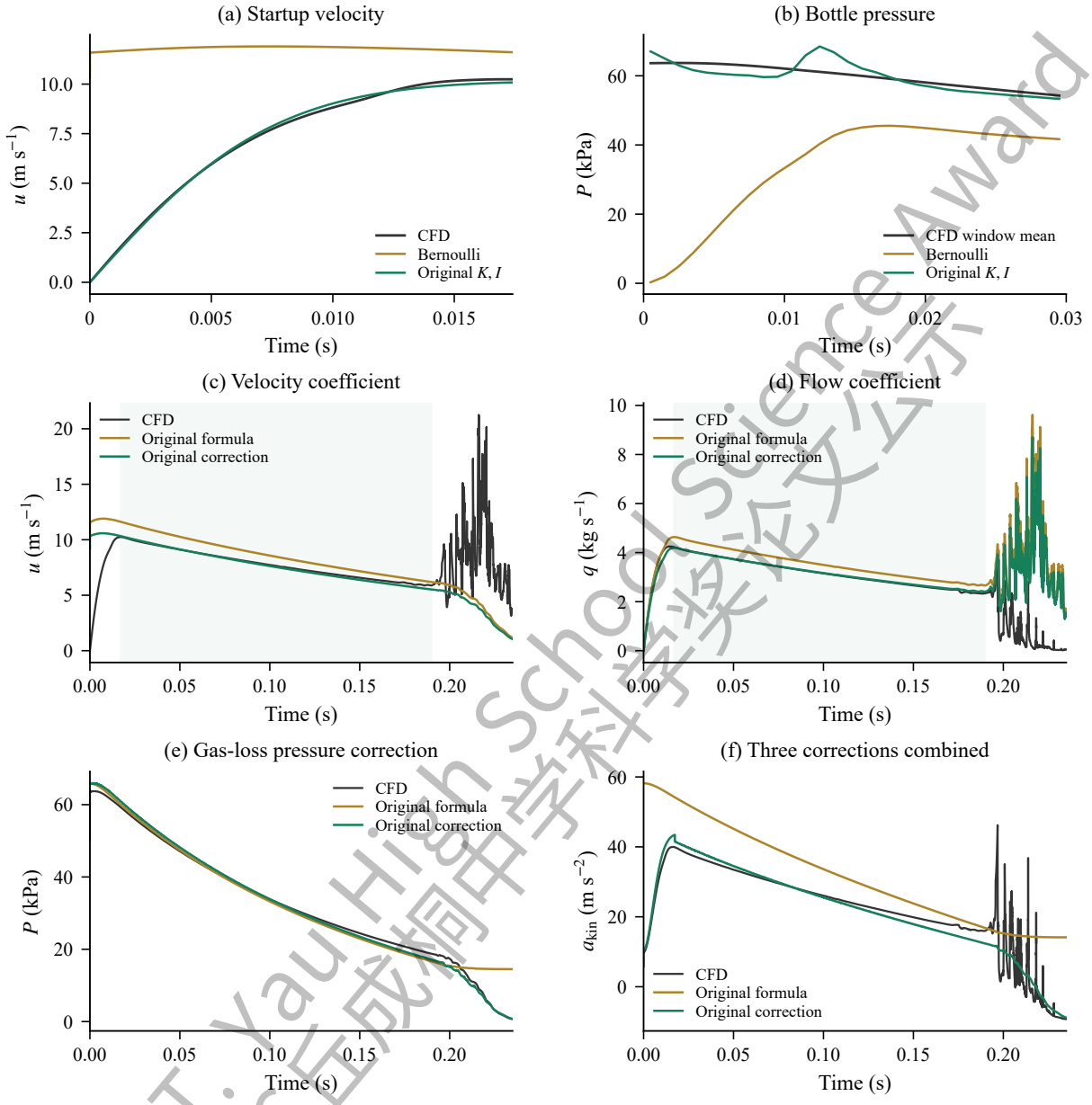


Figure 8-4. Comparison of the original and corrected models with Case B, with all fitted coefficients fixed. (a) Startup velocity calculated from CFD pressure using the original inertance and loss coefficients. (b) Pressure calculated over 1 ms windows. (c) Velocity calculated from CFD pressure with and without the original velocity coefficient. (d) Mass flow rate calculated from CFD velocity with and without the original flow coefficient. Shading in (c) and (d) marks the Case B phase II interval used in Table 8-4. (e) Pressure from the original expansion relation and the gas-mass-loss correction. (f) Acceleration from the original formulas and the three-correction combination. Wherever a body-force head is required, $b = g + a_{\mathrm{kin,calc}}$ is obtained from the corresponding calculation and fed back self-consistently.

2026 S.T. Yau High School Science Award
仅用于2026丘成桐中学科学奖论文公示

8.5 Implications for Simplified Numerical Calculations

Over 0.03- 0.14 s, the time-averaged bottle pressure, remaining water mass, outlet mass flow rate, outlet velocity, derived thrust, and kinematic acceleration differ by up to 4.01% between Cases A and B. The full-record thrust integral differs by approximately 4.24%. Neglecting rocket-acceleration feedback may therefore be acceptable when these averages and the thrust integral are the calculation targets and differences of this size are acceptable.

Feedback also changes interface deformation, delays gas-passage formation and the departure from the liquid mass-flow relation, and shortens the late fluctuation interval. It changes when the velocity, mass flow rate, and acceleration fluctuate, as well as the size and duration of those fluctuations. Similar thrust integrals therefore do not imply similar internal flow. In Case B, the startup inertia and loss correction reduces pressure error, the liquid-phase coefficients reduce velocity and mass flow rate errors, and the gas-loss correction reduces pressure error. These corrections can be retained for the tests and intervals evaluated here.

9 Discussion

9.1 Applicable Phases and Physical Meaning of the Corrections

Table 9-1. Conclusions for the individual corrections in baseline Case A

Specific correction	Test result	Use in this study
Liquid inertia and flow losses added to the pressure formula	Marked improvement in early pressure agreement	Startup pressure calculation
Velocity multiplied by C_v; mass flow rate by C_q	Phase 2 errors reduced by 93.9% and 95.7%, respectively	Local liquid-phase relations
Density reduced uniformly over the full record	Mass flow rate RMSE decreases, but velocity RMSE increases	Not adopted
Gas mass ratio added to the pressure formula	Marked reduction in full-record pressure error	A relation for pressure at later times
Full process fitted with three constants	Negative water mass or late velocity mismatch	Not adopted

These results also show that the corrections K and C_v should not be superimposed, because they are different ways of describing similar losses. The combination of inertia and losses during startup and the constant corrections during liquid-phase flow can explain the data within their respective intervals of applicability. The full-record acceleration calculation in Section 8 still uses the CFD remaining water mass and the gas-loss estimate derived from the CFD mass reports.

9.2 Unresolved Physical Mechanisms and Numerical Errors

The physical interpretation of the brief velocity and acceleration pulses after the gas- liquid transition, and their sensitivity to numerical settings, remain unresolved. Simple corrections to the conventional velocity and mass flow rate formulas can obviously not reflect the transient fluctuations in the CFD results. A study of the decay in CFD water mass and the integral of the derived thrust in each phase, however, reveals that, although outlet velocity and acceleration often fluctuate and reach high instantaneous values in phases 4 and 5, they are very short-lived and make a smaller contribution to the full-record thrust integral than the continuous liquid-phase interval. The calculated expelled water mass and thrust integral for each phase should be compared with the corresponding CFD values in Table 9-2. It is also necessary to make comparisons between interface images and time histories for predictions of interface motion and transient peaks.

There are also limitations on the measurements that can be used for the flight comparison. Only one record of sensor and two independent trials of videos are used. Video acceleration is calculated from position data over a five-frame window spanning approximately 66.7 ms. Uncertainties also arise from image calibration, marker location, axis-angle estimation, and approximate time alignment.

2026 Siyuan High School Science Award
仅用于2026年思源高中科学论文公示

Table 9-2. Cumulative contributions in baseline Case A using the original analysis intervals

Phase	Decrease in water mass / g	Thrust integral / (N·s)	Share of full-record thrust integral
1	52.912	0.9044	11.0%
2	437.004	5.8925	72.0%
3	22.447	0.2506	3.06%
4	91.686	1.0466	12.8%
5	1.960	0.0586	0.715%
6	2.328	0.0348	0.425%

10 Conclusions

This study combines flight measurements, CFD of the internal flow, and tests of simplified formulas, with emphasis on correcting the conventional calculation method. The sensor record and two Tracker trials provide comparisons of the overall first-stage acceleration trend, while their limited time resolution and approximate alignment prevent direct validation of the brief CFD fluctuations. The main conclusions are as follows.

First, the quasi-steady pure-liquid approximation does not apply throughout discharge. At startup, pressure is already present while the liquid is still accelerating. Adding inertia and losses reduces the RMSE of the 1 ms mean pressure over 0- 0.152 s from 15.42 to 1.211 kPa, showing the need to account for startup inertia.

Second, the conventional relations remain applicable during continuous liquid-phase flow after coefficient correction. Using CFD pressure as input, a velocity coefficient of 0.89234 reduces velocity RMSE by approximately 93.9%. Using CFD velocity as input, a mass flow rate coefficient of 0.90487 reduces mass flow rate RMSE by approximately 95.7%. The combined relations fitted over this interval predict an end-of-phase water mass within approximately 1.280 g of CFD.

Third, at later times, the mean outlet velocity can no longer be interpreted as the velocity of a uniform pure-water outflow. At the CFD outlet-velocity peak, the pure-water formula predicts approximately 15.16 kg/s, compared with 0.111 kg/s in CFD.

Fourth, adjusting the expansion exponent alone does not explain the late pressure decrease. Adding the gas-loss term reduces the full-record pressure RMSE from 4.246 to 1.248 kPa, a greater reduction than adjusting the expansion exponent alone. This pressure correction remains conditional on the gas mass loss calculated from CFD data. In the corrected velocity and mass flow rate relations, density cancels from the pressure-driven part of their product, while the hydrostatic part retains its density dependence.

Fifth, cumulative results must be checked when selecting formulas. Some full-record constant-coefficient combinations with relatively low errors nevertheless give negative water mass and should be rejected. The thrust integral is less sensitive to the brief late peaks than to the sustained liquid-phase discharge. However, calculations must still reproduce the water expelled and thrust integral over each phase, including the gas-liquid mixing interval.

Sixth, rocket-acceleration feedback changes the time-averaged bottle pressure, remaining water mass, outlet mass flow rate, outlet velocity, derived thrust, and kinematic acceleration over 0.03- 0.14 s by up to 4.01%, and the full-record thrust integral by approximately 4.24% in the present cases. Neglecting feedback may be acceptable when these quantities are the calculation targets and these differences are acceptable, but feedback delays gas-passage formation and changes the amplitude and duration of late fluctuations. The original startup inertia and loss correction, liquid-phase coefficients, and gas-loss correction remain effective in the Case B tests and intervals evaluated here.

References

[1] J. M. PRUSA, "Hydrodynamics of a Water Rocket," *SIAM Review*, Vol. 42, No. 4, 2000, pp. 719- 726.

[2] G. A. FINNEY, "Analysis of a Water-Propelled Rocket: A Problem in Honors Physics," *American Journal of*

2026 Shi Yan Li Gao School Science Award
仅用于2026年成都市科学奖公开

Physics, Vol. 68, No. 3, 2000, pp. 223- 227.
[3] C. J. GOMMES, "A More Thorough Analysis of Water Rockets: Moist Adiabats, Transient Flows, and Inertial Forces in a Soda Bottle," *American Journal of Physics*, Vol. 78, No. 3, 2010, pp. 236- 243.
[4] A. ROMANELLI, I. BOVE, AND F. GONZÁLEZ MADINA, "Air Expansion in a Water Rocket," *American Journal of Physics*, Vol. 81, No. 10, 2013, pp. 762- 766.
[5] D. N. JOHNSTON, "Prediction of Fluid Inertance in Nonuniform Passageways," *Journal of Fluids Engineering*, Vol. 128, No. 2, 2006, pp. 266- 275.
[6] B. B. MONTEIRO, "Water Rocket," *OpenMDAO/Dymos Documentation*, Ver. 1.11.0.
[7] C. W. HIRT AND B. D. NICHOLS, "Volume of Fluid (VOF) Method for the Dynamics of Free Boundaries," *Journal of Computational Physics*, Vol. 39, No. 1, 1981, pp. 201- 225.
[8] O. UBBINK AND R. I. ISSA, "A Method for Capturing Sharp Fluid Interfaces on Arbitrary Meshes," *Journal of Computational Physics*, Vol. 153, No. 1, 1999, pp. 26- 50.
[9] F. R. MENTER, "Two-Equation Eddy-Viscosity Turbulence Models for Engineering Applications," *AIAA Journal*, Vol. 32, No. 8, 1994, pp. 1598- 1605.
[10] R. WATANABE, N. TOMITA, AND T. TAKEMAE, "Thrust Characteristics of Water Rocket and Their Improvement," *Journal of the Japan Society for Aeronautical and Space Sciences*, Vol. 51, No. 593, 2003, pp. 314- 320.
[11] K. YONEMOTO, T. HIMENO, AND Y. OSHIKATA, "Experiment and Numerical Calculation on Air-Water Phased Propulsion Flow of Water Rocket," *Proceedings of the KSAS- JSASS Joint International Symposium on Aerospace Engineering*, 2008, pp. 375- 378.
[12] N. TOMITA, R. WATANABE, AND A. V. NEBYLOV, "Hands-on Education System Using Water Rocket," *Acta Astronautica*, Vol. 61, No. 11- 12, 2007, pp. 1116- 1120.
[13] G. F. MARRANGHELLO, M. M. LUCCHESE, AND F. S. DA ROCHA, "Analysis of the Propulsion Phase of Water Rockets Using Smartphone Sensors and Video Analysis," *The Physics Teacher*, Vol. 60, No. 6, 2022, pp. 437- 440.
[14] E. E. YANG AND B. L. HOUSTON, "Understanding the Physics of Water Rockets Using Wireless Sensors," *Proceedings of the 2016 IAJC/ISAM Joint International Conference*, 2016, ISBN 978-1-60643-379-9.
[15] H. HUANG, K. LIU, AND D. RANGA, "A Physics-Informed Neural Network Framework for Multiphase Flow Modeling and Parameter Optimization in Water Rocket Systems," *Machine Intelligence and Digital Applications*, IOS Press, 2026.
[16] F. Y. CHANG AND H. C. WENG, "Dynamic Characteristic Analysis of a Two-Stage Water Rocket in Flight," *Journal of the Chinese Society of Mechanical Engineers*, Vol. 41, No. 5, 2020, pp. 605- 614.
[17] B. D. MARCUS, *Theory and Design of Variable Conductance Heat Pipes*, NASA CR-2018, 1972.
[18] A. SAVITZKY AND M. J. E. GOLAY, "Smoothing and Differentiation of Data by Simplified Least Squares Procedures," *Analytical Chemistry*, Vol. 36, No. 8, 1964, pp. 1627- 1639.

Appendix A Record of Experimental Materials

Experimental platform: two-stage water rocket with parachute and pressure-differential separator
Video measurements: fixed camera and yellow tape attached to the rocket as a tracking marker
Sensor kit: ESP32 development board with Type-C port and CH340
GY-521 MPU6050 module
BMP388 digital barometric pressure sensor with IIC interface terminals
MicroSD card module with SPI interface

2026 S.T.Yau High School Science Award
仅用于2026丘成桐中学科学奖论文公示

MicroSD memory card (8 GB)

18650 lithium battery, 3.7 V, 2400 mAh

KCD1 push-button switch

Dupont connector socket (2 rows × 5P pins)

Custom EPE pearl-foam board (length 1 m × width 50 cm × thickness 30 cm)

Appendix B Data Acquisition Program

test.ino

Appendix C Experimental Video Materials

rocket test.mp4

Tracker trial 1: exp1/videos/video(1).mp4

Tracker trial 2: exp2/videos/video(2).mp4

Note: The 2 atmospheres mentioned in the video is the pump pressure-gauge reading, which differs from the actual gauge pressure. When the rocket was pressurized with the pump and measured with a separate pressure gauge, a pump-gauge reading of 2 atm corresponded to an actual gauge pressure of 0.65 atm. This paper uses 0.65 atm as the initial gauge pressure.

Appendix D Data Post-Processing Programs

processdata.py

real a.py

Tracker projects: Experiment_01.trz and Experiment_02.trz. Each archive contains the video, processed position data, spatial and time calibration, and the fitted axis-angle expression used to calculate a_axis.

Appendix E Flight Measurement Data

test1.csv

Tracker results: Experiment_01_results.txt and Experiment_02_results.txt. Columns contain aligned time, horizontal and vertical position, axial acceleration a_axis, and video frame number.

Plotting records: sensor_points_plotted.csv and tracker1_plot.csv / tracker2_plot.csv. The omitted sensor and video points are listed separately in excluded_sensor_points.csv and Experiment_02_omitted.csv.

Appendix F Simulation Data and Animations

accel-rfile.out (CFD-derived acceleration)

average-p-rfile.out (mean pressure inside the bottle)

average-velocity-rfile.out (area-weighted mean axial outlet velocity)

flowrate-rfile.out (mass flow rate at the bottle outlet)

masswater-rfile.out (water mass inside the bottle)

p-gauge-rfile.out (gauge pressure at the bottle outlet, P_{gauge})

thrust-rfile.out (derived thrust)

pressure.mov

temperature.mov

water.mov

Appendix G Grid, Time-Step, and Iteration Sensitivity Test Results

Grid-independence test results

Time-step-independence test results

Iteration-sensitivity test results

2026 C. T. Yau High School Science Award
仅用于2026丘成桐中学科学奖论文公示

致谢页

本研究起源于我们对航空航天的兴趣.我们平时经常关注火箭发射,也在课内物理学习中接触到了伯努利原理等流体力学知识.由此,我们开始好奇:能否利用已经学过的知识,建立一套描述水火箭运动的公式?更重要的是,这些公式究竟能在多大程度上描述真实水火箭的飞行过程?如果理论与实际存在差异,原因又是什么?带着这些问题,我们共同确定了研究选题.考虑到嵇海锐此前已有 CFD 仿真研究经验,我们决定结合实验、数值仿真与理论分析开展研究.

本研究的指导老师为于小雨老师,是本校物理教师,也是我们的 IYPT 指导老师,但并非我们的课内物理授课教师.老师为我们主要提供方向性意见,在论文撰写阶段未进行额外指导,指导为无偿指导.此外,在火箭飞行实验中,我们曾邀请徐梓桐同学协助实验操作.我们感谢老师和这位同学在研究过程中给予的帮助.

选题确定后,装置采购与火箭组装由我们共同完成.研究初期遇到的第一个困难,是火箭加压后出现漏气,无法正常开展实验.经过排查,我们发现所选瓶子的瓶口与两级连接器不匹配,更换后才解决这一问题.这让我们意识到,研究计划与实际实验之间,还隔着许多需要逐一处理的具体问题.

为了获取飞行数据,我们购买并组装了传感器系统,随后开展编程与调试.这部分工作主要由嵇海锐负责.过程中遇到的问题包括供电连接在振动条件下不稳定、IMU 零位漂移,以及数据写卡造成的程序阻塞等.我们分别通过调整连接方式、重新获取静止零位参考,以及调整数据读取和记录的程序结构进行处理,相关问题与处理过程已在论文第三部分中说明.

传感器调试与飞行实验交替进行,因为一些问题只有在实际飞行条件下才会暴露.袁昊琨主要负责火箭维护,试飞实验由我们共同完成.实验过程中,令我们印象最深的一次挫折,是火箭二级在飞行中突然偏转,挂在了一棵很高的树上,当天未能取回.由于传感器全部安装在上面,我们一度担心研究会因此中断.直到第二天取回火箭,我们才发现,尽管经历了一夜雨淋,传感器仍在持续运行.这一结果让我们感到意外,也让我们对这套系统在此次意外中的表现有了更直观的认识.

获得一组可用于分析的飞行数据后,嵇海锐负责数据后处理;袁昊琨同步查阅文献,构建并核查传统理论计算方法.与此同时,嵇海锐开展 Fluent 仿真工作.这一阶段遇到的主要困难,是按照打气筒压力表的读数设置初始压力后,仿真结果与实验明显不符.我们最初记录的压力表读数为 2 atm,随后通过独立压力表复测,发现对应的实际读数约为 0.65 atm,并与商家确认了原压力表存在偏差.这一经历使我们认识到,测量设备给出的读数也需要核查,不能直接将理论与实验之间的所有差异归因于模型本身.

获得完整的仿真数据后,我们将其与后处理后的实验数据进行对比,评估二者的一致性,并在此基础上推进理论公式的修正与分析.公式修正工作主要由嵇海锐负责,袁昊琨则结合前期文献阅读与研究进展,起草文献综述.

理论分析完成后,我们开始集中撰写论文.袁昊琨负责文献综述初稿及前期相关草稿;嵇海锐在这些草稿的基础上,完成实验、数值仿真和理论分析三部分的主体撰写;袁昊琨随后对论文内容进行审核、修正,并承担排版工作.上述分工贯穿研究与写作过程,双方在共同开展的工作中持续讨论,并根据实验和分析结果调整研究思路.

本研究使用的 AI 工具包括 ChatGPT 和 Gemini.我们在下文说明其具体用途:

在传感器系统搭建与调试阶段,由于我们缺乏电路连接和焊接经验, GPT-5.6 和Gemini 3.6(和3.1pro) ,在方案理解、接线问题及相关操作知识方面提供了重要帮助.我们也缺乏使用 Arduino IDE 编写程序的经验,因此,这两种工具为传感器程序编写提供了关键支持,并持续参与调试过程中有关程序问题的分析和修改.

在数据分析阶段,多份用于数据后处理和数据拟合的 Python 程序主要由上述 AI 工具辅助编写.具体涉及火箭轴向方向提取,原数据绘图等.这些工具在代码生成与修改方面承担了较多工作.

论文撰写阶段尝试过使用GPT-5.6 检索论文并完成文献综述.但最终未采纳,检索到的文献对论文撰写构成参考.

在论文整理阶段,GPT-6 协助完成了 Word 文稿的PDF 排版,包括图表、图注及相邻说明的分页调整,以及转换后的内容完整性检查.

我们感谢指导老师、协助实验的同学,以及研究过程中给予我们帮助的人.这项研究让我们体会到,从一个出于兴趣的问题出发,到获得数据、解释差异并形成论文,需要反复尝试,也需要如实记录那些未能奏效的尝试和得到的帮助.

2026 IYPT 中国赛区 High School Award 仅用于论文提交展示